

1 **Chaos, storms, and climate on Mars**

Edwin S. Kite,^{1,2} Scot Rafkin,³ Timothy I. Michaels,³ William E. Dietrich,¹
and Michael Manga.^{1,2}

¹Earth and Planetary Science, University
of California Berkeley, Berkeley, California,
USA.

²Center for Integrative Planetary Science,
University of California Berkeley, Berkeley,
California, USA.

³Department of Space Studies, Southwest
Research Institute, Boulder, Colorado, USA.

arXiv:1101.0253v1 [astro-ph.EP] 31 Dec 2010

Abstract. Channel networks on the plateau adjacent to the Juventae outflow channel source region and chaos have the highest drainage densities reported on Mars. We model frozen precipitation on the Juventae plateau, finding that the trigger for forming these channel networks could have been ephemeral lakeshore precipitation, and that they do not require past temperatures higher than today. If short-lived and localized events explain some dendritic channel networks on Mars, this would weaken the link between dendritic valley networks and surface climate conditions that could sustain life. Our analysis uses Mars Regional Atmospheric Modeling System (MRAMS) simulations and HiRISE Digital Terrain Models. Following a suggestion from *Mangold et al.* [2008], we model localized weather systems driven by water vapor release from ephemeral lakes during outflow channel formation. At Juventae Chasma, the interaction between lake-driven convergence, topography, and the regional wind field steers lake-induced precipitation to the southwest. Mean snowfall reaches a maximum of 0.9 mm/hr water equivalent (peak snowfall 1.7 mm/hr water equivalent) on the SW rim of the chasm. Radiative effects of the thick cloud cover raise mean plateau surface temperature by up to 18K locally. The key result is that the area of maximum modeled precipitation shows a striking correspondence to the mapped Juventae plateau channel networks. Three independent methods show this fit is unlikely to be due to chance. We use a snowpack energy balance model to show that if the snow has the albedo of dust (0.28), and for a solar luminosity of 0.8 ($\equiv 3.0$ Gya), then if the atmospheric greenhouse effect is unchanged from today only

25 0.4% of lake-induced precipitation events produce snowpack that undergoes
26 melting (for a 6K increase in the atmospheric greenhouse effect, this rises
27 to 21%). However, warming from associated dense cloud cover would allow
28 melting over a wider range of conditions. Complete melting of the snow from
29 a single event is sufficient to move sand and gravel through the observed chan-
30 nel networks. At Echus Chasma, modeled precipitation maxima also corre-
31 spond to mapped plateau channel networks. In these localized precipitation
32 scenarios, global temperatures need not be higher than today, and the rest
33 of the planet remains dry.

1. Introduction

34 The highlands of Mars show both erosional and depositional evidence for past fluvial
35 flow, and geochemical and textural evidence at Meridiani indicates these features were
36 formed by liquid water [*Malin & Edgett, 2003; Kraal et al., 2008a; Murchie et al., 2009a;*
37 *Grotzinger et al., 2006; McLennan & Grotzinger, 2008*]. The distribution of fans and chan-
38 nels with elevation, together with their morphology and inferred discharge, argue against
39 groundwater as the sole source, and demand precipitation [*Carr & Head, 2003, 2010;*
40 *Hynek & Phillips, 2003*]. Three models may explain these observations. (1) A globally
41 prolonged climate interval that intermittently allowed surface runoff is the most straight-
42 forward interpretation, and one that can draw on knowledge of arid and polar Earth
43 analogs [*Halevy et al., 2007; Barnhart et al., 2009*]. (2) Water vaporised by impacts would
44 briefly warm the global atmosphere, and precipitation from these transient water vapor
45 greenhouse atmospheres could cut some valleys where there is evidence of rapid discharge
46 [*Segura et al., 2002, 2008; Kraal et al., 2008b; Toon et al., 2010*]. In addition, ancient
47 channels are patchily distributed [*Williams, 2007; Weitz et al., 2008; Fassett & Head,*
48 *2008a; Hynek et al., 2010; Carr & Malin, 2000*], which suggests (3) localized precipitation
49 as an alternative to transient, or prolonged, global wet conditions.

50 Localized precipitation is especially attractive as an explanation for channels exposed by
51 erosion of layered deposits on the Valles Marineris plateau ~ 3.0 Gya [*Mangold et al., 2004;*
52 *Weitz et al., 2008*], and also fans at Mojave Crater ~ 10 Mya [*Williams & Malin, 2008*].
53 That is because these channels and fans postdate the sharp decline in globally-averaged
54 erosion rates, aqueous alteration, and channel formation near the Noachian - Hesperian

55 boundary [Murchie et al., 2009a; Fassett & Head, 2008b; Golombek et al., 2006]. The
56 rarity of channels, fans, erosion, or aqueous minerals of similar age suggests that the
57 Valles Marineris plateau channel networks and Mojave Crater fans do not record global
58 episodes of surface runoff. Localized precipitation is an alternative, with vapor sourced
59 from a transient event such as groundwater release during chaos terrain formation (at
60 Valles Marineris) or partial melting of an ice-silicate mixture during impact (at Mojave
61 Crater). This has previously been suggested, but never modeled [Mangold et al., 2008;
62 Williams & Malin, 2008].

63 Here we report our study of the best-preserved of the Valles Marineris plateau channel
64 networks, west of Juventae Chasma [Malin et al., 2010; Weitz et al., 2010]. The Juventae
65 plateau networks include “hillslope rills and low-order streams,” leading Malin et al. [2010]
66 to describe them as “the best evidence yet found on Mars to indicate that rainfall and
67 surface runoff occurred.” In §2-3, we summarize geologic observations: some constitute
68 boundary conditions for the model, others are targets that the model must reproduce in or-
69 der to be considered successful. In §4 we analyse results from Mars Regional Atmospheric
70 Modeling System (MRAMS, Rafkin et al. [2001]; Michaels et al. [2006]) simulations of
71 chaos flood-effect precipitation that include detailed cloud microphysics (Appendix A).
72 We find excellent agreement between the model-predicted precipitation locations and the
73 previously-mapped area of layered deposits and inverted channel networks. In this paper,
74 we concentrate on what controls the rate and location of precipitation. A companion
75 paper, Kite et al. [in review] (available at <http://arxiv.org/abs/1012.5077>) – henceforth
76 ‘Paper 1’ – describes idealized simulations of cloud formation and precipitation in a thin,
77 cold atmosphere perturbed by a lake. Precipitation in our model falls as snow, but the

78 geologic observations demand liquid water runoff. Snowpack melting on the Juventae
79 plateau will occur under certain combinations of orbital parameters and snowpack phys-
80 ical properties. These are determined (§5) by running a simple snowpack thermal model
81 over all seasons, all plausible solar luminosities, and for the full range of orbital conditions
82 sampled by the chaotic diffusion of Mars' orbital parameters [*Laskar et al.*, 2004]. We
83 calculate the probability that snowpack melting will occur as a function of solar luminos-
84 ity and additional greenhouse effect. In §6, we evaluate multiple working hypotheses for
85 the mechanism of channel formation. We compare these hypotheses to data from a small
86 number of key localities on the Juventae Plateau. We do not carry out a comprehensive
87 geologic analysis. Finally we test the localized-precipitation hypothesis at a second site,
88 Echus Chasma (§7), and consider the implications of localized precipitation for global
89 excursions to conditions warmer than the present-day on Hesperian Mars (§8).

2. Geologic constraints: Valles Marineris plateau channel networks

90 The Valles Marineris plateau layered deposits are distinct from layered deposits elsewhere
91 on Mars [*Weitz et al.*, 2008; *Murchie et al.*, 2009a; *Weitz et al.*, 2010]. Dendritic channels
92 with both positive and negative relief are commonly found in association with the plateau
93 layered deposits [*Malin & Edgett*, 2003; *Edgett*, 2005; *Williams et al.*, 2005], with preserved
94 drainage densities as high as 15 km^{-1} and commonly $>1 \text{ km}^{-1}$. In contrast, most Mars
95 light-toned layered deposits (LLD) have few or no channels visible from orbit. Channels
96 at different levels within the plateau layered deposits crosscut one another [*Weitz et al.*,
97 2010]. This requires that plateau channel formation was either interspersed with, or
98 synchronous with, the depositional events that formed the layers, and suggests a common
99 geologic scenario for channel formation and plateau layered deposit formation. Opal (\pm

hydroxylated ferric sulfate) has been reported in the plateau layered deposits [Milliken
et al., 2008; Bishop et al., 2009], whereas most Mars LLD show sulfate (\pm hematite \pm
phyllosilicates) [Murchie et al., 2009a]. Plateau layered deposits show no evidence for
regular bedding, while most LLD give the visual impression of quasi-periodic bedding,
which has been statistically confirmed at many locations [Lewis et al., 2008, 2010]. Because
the most likely pacemaker for quasi-periodic sedimentation is orbital forcing [Kuiper et
al., 2008b; Lewis et al., 2008], this suggests the process that formed the plateau layered
deposits was not sensitive to orbital forcing. This could be because stochastic processes
controlled deposition, or because deposition timescales were much shorter than orbital
timescales [Lewis et al., 2010]. The deposits are thin, no more than a few tens of meters
total thickness [Weitz et al., 2010], in contrast to the many km of sulfate-bearing deposits
that accumulate within craters and canyons. Some show pitted surfaces that Le Deit
et al. [2010] relate to the ice-rich dissected mantle terrain of the northern midlatitudes.
Stratigraphy constrains the opaline plateau layered deposits to be early Hesperian or
younger, so they are among the youngest classes of aqueous minerals on Mars [Murchie
et al., 2009a], and significantly postdate the maximum in valley formation during the
Late Noachian – Early Hesperian [Le Deit et al., 2010]. Taken together, these differences
suggest the process which formed the Valles Marineris plateau layered deposits differed
from that forming layered deposits elsewhere on Mars [Murchie et al., 2009a].

The plateau layered deposits and inverted channels formed over an extended interval
of time. Tilted channels are present on downdropped fault blocks [Le Deit et al., 2010],
and some channels are truncated by chasm edges. This shows that some channels formed
before backwasting of the chasm to its present day form. Crosscutting streams exposed at

123 different levels within the plateau layered deposits confirm that multiple periods of runoff
124 are recorded on the plateau [*Weitz et al.*, 2010].

125 These observations raise several questions. What was the geologic context of plateau
126 layered deposit formation? What was the source of the water for channel formation, and
127 what permitted surface liquid water at this location? Does this require atmospheric pres-
128 sures, temperatures, or water vapor loading different from contemporary Mars – and if
129 so, are the required changes global, regional or local? What were the mechanics of chan-
130 nel formation - for example, are these mechanically-eroded or thermally-eroded channels?
131 Our focus in this paper is on the first three questions, although we do report some mea-
132 surements relevant to channel formation mechanisms in §6.

133 Channels are usually found on plateaux immediately adjacent to chasms, suggesting
134 that location on a plateau immediately adjacent to a chasm provided a driver (limiting
135 factor) for channel formation and/or preservation (Figure 1a). For example, the Echus,
136 Juventae and Ganges plateau channel networks are all immediately West (downwind) of
137 inferred paleolakes (Figure 2; *Coleman & Baker* [2007]; *Harrison & Chapman* [2008]). A
138 relief-elevation plot confirms, independently, that all light-toned layered deposits are on
139 the plateau near the edge of a chasm (Figure 2). To form, a channel requires water supply
140 sufficient to balance continuous losses to infiltration and evaporation, while generating
141 runoff. Runoff must encounter sediment that is fine-grained enough to be mobilized.
142 Inverted channels have additional requirements: to be exposed at the surface today, an
143 inverted channel must be preferentially cemented or indurated, and then incompletely
144 eroded. Therefore, there are five potential limiting factors for inverted channel formation:

145 - heat, water, sediment, cementing fluids, or erosion. Location downwind of a chasm
146 should logically supply at least one.

147 We hypothesize that the Juventae, Echus and Ganges plateau channel networks formed
148 downwind of ephemeral chaos lakes, through precipitation from lake-effect storms (Paper
149 1, Figure 3). The spatial association between chasm lakes and plateau channels/light-
150 toned deposits can then be explained if rain or snow from nearby lakes is the limiting
151 factor for forming plateau channels and light-toned deposits. This is analogous to the
152 ‘snowbelts’ that form downwind of the Great Lakes of N America from the cumulative
153 precipitation of lake-effect storms (Figure 1b). Our hypothesis predicts that simulations
154 of lake-effect storms in Valles Marineris should produce precipitation that is localized
155 to the chasm rim and in the observed locations. We test our hypothesis at Juventae
156 Chasma, because it has the best-preserved plateau channels and the geologic evidence
157 for a paleolake there is also compelling [Coleman & Baker, 2007; Harrison & Chapman,
158 2008]. Other possible scenarios for forming plateau channels and plateau layered deposits
159 (Figure 3) are discussed in §6.

3. Geologic constraints: Boundary conditions at Juventae Chasma

160 Juventae Chasma has a spillway at $\approx +1$ km elevation that is connected to the Maja Vallis
161 outflow channel (Catling *et al.* [2006]; Coleman & Baker [2007]; Figure 4). The floor of
162 Juventae Chasma is below -4 km. Insofar as material was removed from the chasm by
163 fluvial or debris-flow transport across the spillway, this suggests that a lake many km
164 deep existed at least once in Juventae Chasma [Coleman & Baker, 2007]. Evidence
165 that multiple outbursts cut Maja Vallis also suggests that Juventae Chasma was flooded
166 multiple times [Harrison & Grimm, 2008].

167 The duration of groundwater outburst floods depends on the permeability of the source
168 aquifer, which is unknown. *Harrison & Chapman* [2008] calculate a duration of 0.1 –
169 10^5 days per event, with $\leq 5 \times 10^3$ days per event preferred. The corresponding peak
170 discharge rates are $3 \times 10^5 - > 10^8 \text{ m}^3\text{s}^{-1}$. When discharge falls below the evaporation rate,
171 icing-over of the lake surface is increasingly likely. For the 140 km-diameter cylindrical
172 chaos modeled by *Harrison & Chapman* [2008], and an evaporation rate of 2 mm/hr,
173 the cryosphere fractures are frozen shut before the discharge falls below the evaporation
174 rate. Alternatively, surface liquid water in a chaos terrain can be generated by failure of a
175 dam confining an ice-covered lake, leading to mechanical disruption of the ice cover. For
176 example, the 2002 stepwise collapse of Antarctica’s Larsen B ice shelf took 3 weeks, with
177 open water between collapsed ice blocks (Figure 5; *Scambos et al.* [2003]).

178 Boundary conditions are as follows. We parameterize the dependence of lake surface
179 roughness on wind speed following *Garrett* [1992]. We impose a lake temperature of
180 278.15K (5°C), which is midway between dissipative throttling (Joule-Thompson) heat-
181 ing of aquifer water initially at 5km, and two-phase hydrostatic ascent [*Gaidos & Marion,*
182 2003]. However, for the largest lake simulated (`juventae_high`, Table 1), we set lake sur-
183 face temperature to 273.15K (0°C). This is because the high latent-energy flux associated
184 with a relatively high temperature and a large lake area caused numerical instabilities
185 in the model. We hold lake temperature steady. This is a reasonable assumption if the
186 atmospheric response timescale (hours-days) is shorter than the timescale over which the
187 chaos flood hydrograph changes, or if surface water continuously pours over the spillway,
188 allowing the surface layer to be refreshed by warmer water from depth. Wind-dependent
189 lake surface roughness is from equation 7.21 of *Pielke* [2002]. The inverted streams at

190 Juventae required surface liquid water to form, but currently the low atmospheric pres-
191 sure at plateau elevation (+2 km) makes surface liquid water unstable [*Conway et al.*,
192 2010]. Therefore, we doubled initial and boundary pressure throughout our simulation.
193 Doubling pressure halves the peak wind speed obtained by full release of Convectively
194 Available Potential Energy (CAPE) (Paper 1). Therefore, it is conservative in terms of
195 localized precipitation, because ascent of air parcels to cold altitudes will be less rapid
196 (Paper 1). We use present-day topography in our model, apart from flooding to the
197 lake level within Juventae Chasma. A minor exception is that we remove the sulfate-
198 bearing [*Bishop et al.*, 2009; *Catling et al.*, 2006] light-toned layered deposits from within
199 the chasm, which would otherwise form islands in our ephemeral lake. This is because
200 we agree with the geologic interpretation that these deposits largely postdate chasm for-
201 mation [*Murchie et al.*, 2009b], although there is disagreement on this point [*Catling et*
202 *al.*, 2006]. The change has no effect on our best-fit model (`juventae_high`) because, in
203 our smoothed topography, the lake level in `juventae_high` is higher than the summits
204 of the sulfate-bearing light-toned layered deposits. We use present-day solar luminosity
205 in our precipitation model (but not in our melting model; §5). This is conservative in
206 terms of localized precipitation, because lower atmospheric temperatures favor localized
207 precipitation (Paper 1). More details of the model setup are provided in Appendix A.

4. Juventae mesoscale model: precipitation output

208 This paper reports the results of model runs that vary lake temperature and lake level
209 (Table 1), holding orbital elements and obliquity at present-day values and fixing the
210 season at simulation start to southern Summer ($L_s \sim 270$). An MRAMS run simulating 7
211 days at Valles Marineris takes ~ 0.5 years to complete (wall time), so we are limited in the

212 number of parameters we can vary. In addition, we must rerun the General Circulation
213 Model (GCM) that supplies the mesoscale boundary conditions if we wish to model a
214 major change in pressure or dust loading. This limits the range of sensitivity tests we can
215 practicably apply. Paper 1 describes a wider range of sensitivity tests.

4.1. Analysis of best-fit model

216 *Lake-driven convergence.* The lake perturbation to the atmosphere is superimposed on the
217 complex, topographically driven Valles Marineris mesoscale windfield [*Rafkin & Michaels,*
218 2003; *Spiga & Forget, 2009*]. Strong slope winds are seen at Juventae Chasma in the
219 `juventae_dry` run, as previously described [*Rafkin & Michaels, 2003; Spiga & Forget,*
220 2009]. The diurnal cycle of upslope daytime winds and downslope nighttime winds is
221 broken by the lake, which drives low-level convergence strong enough to overcome the
222 upslope daytime wind (Figure 6b). At altitudes <6 km, the convergence is toward a sheet-
223 like time-averaged updraft running along the lake's long axis (N-S), and concentrated in
224 the southern half of the lake. Above 10 km, wind moves out from this updraft. East-
225 directed outflow encounters the west-directed prevailing wind and slows, allowing more
226 time for ice crystals to precipitate out before reaching the chasm edge. West-directed
227 outflow is much faster. Above 20 km, the windfield is increasingly dominated by radial
228 flow away from a narrow, cylindrical updraft in the center of the lake. Lake storm effects on
229 the background windfield are minor above 40km. The combined effect of a copious water
230 vapor supply, the availability of dust for ice nucleation, water vapor and cloud radiative
231 effects, and induced low-level convergence results in continuous modeled precipitation.

232 *Radiative effects:* Mean temperature rises by 17K downwind of the lake, where icy scat-
233 terers have precipitated but the greenhouse effect of vapor remains (Figure 6c). There is

234 a broad region of $>5\text{K}$ warming. On average, downwelling longwave radiation increases
235 by 60 Wm^{-2} SW of the deep pit W of S Juventae. Ice cloud scattering partly compen-
236 sates for this during the day, but maximum temperature also rises, by up to 8K , which
237 is important for melting (§5). However, in the area of greatest modeled precipitation,
238 maximum temperature is reduced by up to 3K because of the locally high atmospheric
239 ice column abundance.

240 *Water vapor and ice column abundance:* The time-averaged water vapor column abun-
241 dance (Figure 7a) shows that high vapor abundances are confined to the canyon. Ascent
242 of vapor-laden parcels up canyon walls aids crystallization, and ice/total water column
243 mass ratios increase from typically $<50\%$ within Juventae Chasma to $60\text{-}70\%$ on the
244 plateau. Most vapor is found at low elevations. The peak precipitable vapor column
245 abundance is $\sim 0.27 \text{ cm}$ and is located slightly SW of the lake's areal centroid. The peak
246 in time-averaged ice column abundance (Figure 7b) is shifted 30km further WSW. This
247 is the product of plume ascent timescales and the WSW-directed background wind speed
248 (Paper 1). The falloff of ice column abundance with distance from this peak is almost sym-
249 metric. This is because the outward-directed pressure gradient at the top of the buoyant
250 plume is much stronger than that driving the background wind field. The highest water
251 ice column abundances away from the lake are above a promontory jutting into the lake
252 on the SW edge of the chasm, and along the S edge of the chasm. These also correspond
253 to the highest values of precipitation, as discussed below and shown in Figures 8, 9 and
254 10.

255 *Rate and location of snowfall.* The footprint of precipitation is displaced downwind of the
256 centroid of the lake by a distance similar to the product of vapor lifetime (loss due to

ice crystal growth and subsequent gravitational sedimentation) and characteristic wind
velocity at cloud height (Figure 10). Because the size of Juventae Chasma exceeds this
distance, the peak in total precipitation (1.3 mm/hr) lies within the lake. We ignore this
prediction because it cannot be geologically tested, and instead only describe results for
precipitation on land.

Most snow falls close to the chasm edge (Figure 9). Water-ice precipitation on the chasm
flanks has a maximum on a promontory southwest of the lake center. Mean precipitation
is >0.6 mm/hr only in a narrow belt <40 km from the chasm edge on the SW rim of
the chasm. This area of high modeled precipitation corresponds to the mapped area of
channels and layered deposits (Figure 9).

The reduction in snowfall with distance from the chasm is rapid (Figure 11). The
decline is most rapid upwind (east) of the chasm. 200 km east of the chasm rim, peak
snowfall and mean snowfall are both 1000 times less than at the chasm rim. The falloff
is strongly modulated by topography: at a given distance from the lake, plateaux receive
10-100 times more snowfall than canyon floors.

Maximum precipitation on land (not shown) is 1.7 mm/hr. Maximum precipitation
is between 1.5 and 2.0 times the mean rate in the area of greatest precipitation. This
does not include transient high snowfall during model spin-up, immediately after aerosol
microphysics are switched on.

The inflection in precipitation contours at the chasm edge (Figures 10 and 9) is a
projection effect of the steep chasm wall slopes: fall rates per unit column atmosphere
decrease smoothly with distance from the lake, but at the chasm wall the snow from this
column is spread over a larger surface area.

280 Because precipitation is localized and vapor lifetime is short, precipitation rates are
 281 comparable to evaporation rates.

282 *Mass & energy budgets:* The mean evaporation rate found from our mass balance (~ 2
 283 mm/hr, Table 2) entails 1.4 kW/m² evaporative cooling. Is our assumption of constant
 284 lake surface temperature sustainable? 1.4 kW/m² cannot be supplied from a liquid lake
 285 by conduction. Thermal convection may transfer the required heat if lake temperature is
 286 above water's temperature of maximum density (277.13K) and

$$q_{convect} = 0.05 \left(\frac{\rho g \alpha \Delta T}{\kappa \nu} \right)^{1/3} k \Delta T > 1.4 \text{ kW/m}^2 \quad (1)$$

287 where $q_{convect}$ is convective heat flow in W/m², $\rho = 1000$ kg/m³ is water density, $g =$
 288 3.7 m/s² is Mars gravity, $\alpha = 2 \times 10^{-4}$ K⁻¹, $\kappa = 1.4 \times 10^{-7}$ m²/s, $\nu = 10^{-6}$ m²/s, k
 289 = 0.6 W/m/K is thermal conductivity, and ΔT is the temperature difference across the
 290 lake [Postberg et al., 2009]. With $\Delta T = 2.5$ K, we obtain $q_{convect} = 1.8$ kW/m² which can
 291 sustain the evaporation. An isolated, well-mixed lake of depth 5 km would cool only 0.006
 292 K/sol through evaporative cooling, so the assumption of constant lake surface temperature
 293 is reasonable.

294 Evaporitic loss from a fully open lake, 1.3×10^4 m³s⁻¹ (= 1.9 mm/hr) in our best-fitting
 295 model, is small compared to maximum Maja Valles outflow channel discharge (1.1×10^8
 296 m³ s⁻¹; Kleinhans [2005]).

4.2. Sensitivity to flooding depth

297 The location of precipitation is sensitive to flooding depth, and flooding depths close to
 298 the spillway provide the best match to observations (Figure 10). As lake level rises, the

299 offset of maximum precipitation from the lake center changes. The main change on land
 300 as the flooding depth is moved closer to the spillway is that precipitation to the S of
 301 Juventae Chasma is reduced. This is because the area of convergence shifts NW and then
 302 N, tracking the centroid of lake area.

303 More than 80% of vapor released by the lake is trapped in or next to the lake as snow
 304 (Figure 13). As plume intensity increases, so does the fraction of water vapor that snows
 305 out locally. Plume intensity - which we define using updraft velocity and cloud height -
 306 increases with increasing lake size (Paper 1) and with increasing lake temperature. There-
 307 fore, higher flooding depths within Juventae Chasma lead to more localized precipitation.
 308 Atmospheric water does increase with increasing lake area, but slowly (Table 2). Only
 309 `juventae_low` and `juventae_med` are directly comparable because of the lower lake tem-
 310 perature in `juventae_high`.

4.3. Comparison between area of modeled precipitation and area of observed channels

311 We use four independent metrics to quantify the agreement between geologic data and
 312 precipitation model that is qualitatively apparent in Figure 9. Because (i) channels are
 313 exposed by incomplete erosion of the plateau layered deposits, (ii) the inverted channels
 314 are themselves layered, and (iii) channels are found wherever layered deposits are in-
 315 completely eroded on the Juventae plateau, we assume that areas containing light-toned
 316 layered deposits also contain channels.

317 • *Method of Pielke & Mahrer [1978]*. Following *Pielke* [2002], let A_4 be the area of the inmost
 318 grid in the MRAMS domain, $P_{i,t}$ be the area of precipitation predicted by meteorological
 319 model i above some threshold value t , and G_j be the area of channels and light-toned

320 layered deposits (collectively referred to as “geology”, for brevity) mapped using criteria
 321 j . Then the skill of the model in predicting the ancient channels is

$$skill = \frac{F_E}{F_M} = \frac{(P_{i,t} \cap G_j)/G_j}{P_{i,t}/A_4} \quad (2)$$

322 where F_E is the fraction of the geology in areas with model precipitation above the thresh-
 323 old, and F_M is the fraction of the model domain over which the model precipitation is
 324 above the threshold. The fraction of the model-predicted area that is occupied by geol-
 325 ogy, or coverage

$$coverage = (P_{i,t} \cap G_j)/P_{i,t} \quad (3)$$

326 is a measure of the tendency of the model to overpredict the observed geology (where
 327 a value of 1 corresponds to no overprediction). Here, the null hypothesis is that the
 328 association between model and data is due to chance. *skill* and *coverage* are shown in
 329 Table 3. `juventae_high` shows the greatest skill, for both j . We obtain *skill* values >200
 330 for `juventae_high` and $t = 0.8$ mm/hr. For these cases, the area of overlap between
 331 prediction and data is >200 times that expected by chance, showing that the agreement
 332 is almost certainly not due to chance.

333 • *Monte Carlo*. For this metric, we determine the fraction of randomly placed precipitation
 334 templates that provide a better fit to the geologic observations than the modeled precip-
 335 itation. We take the predicted precipitation P for each model i , including snow falling
 336 back into the lake (the precipitation ‘template’), and randomly translate it in latitude and
 337 longitude, wrapping around the boundaries of the inmost model grid (~ 1300 km x ~ 870

338 km). This creates a new modeled precipitation grid Q_i . A data grid G_j is constructed by
 339 assigning 1 to areas containing mapped inverted channels or light-toned layered deposits
 340 and 0 otherwise. We then calculate the cross-correlation as

$$X = G'_j * Q'_i \quad (4)$$

341 where the primes denote normalization (for each trial) by subtracting the nonlake mean
 342 and dividing by the nonlake standard deviation. The area of the present-day lake is
 343 masked out in all cases. We repeat this 10^4 times per model. Here, the null hypothesis
 344 is that the geology formed from a localized source of some kind, but that the location of
 345 this source was uncorrelated with present-day Juventae Chasma. The resulting p-values
 346 are 0.005 for `juventae_high` (nominal $X = 0.476$), 0.009 for `juventae_med` (nominal X
 347 $= 0.365$), and 0.058 for `juventae_low` (nominal $X = 0.044$). These are for the map of *Le*
 348 *Deit et al.* [2010]. The null hypothesis is rejected at the 99.5% level for for `juventae_high`:
 349 if the observed channels and layered deposits formed from a localized source of some kind,
 350 it was almost certainly close to the present-day center of Juventae Chasma.

351 • *Azimuth.* We assign each land pixel to its nearest pixel on the perimeter of the lake.
 352 We then assign each perimeter pixel to its normalized distance along the circumference.
 353 Both the perimeter-matched geologic data and the perimeter-matched model output are
 354 then smoothed with a gaussian kernel of full width at half maximum equal to 5% of
 355 lake circumference. The results are shown in Figure 12. All models produce a broader
 356 distribution of snowfall with azimuth and are also biased counterclockwise (from SW to
 357 S) with respect to the data. This bias is least severe for `juventae_high`. `juventae_high`
 358 also shows the best overall fit to the data: by cyclic translation of the smoothed and

359 area-normalized precipitation pattern, we can find the percentage of perturbed patterns
360 that would provide a better least-squared fit to the smoothed data than our actual model.
361 For the *Le Deit et al.* [2010] (*Weitz et al.* [2010]) geology, this percentage is 7% (10%)
362 for `juventae_high`, 12% (16%) for `juventae_med`, and 36% (39%) for `juventae_low`.
363 (Note that the azimuthal distributions shown in Figure 12 are maximum-normalized, not
364 area-normalized).

365 • *Falloff of precipitation.* Figure 11 shows cumulative distribution functions (CDFs) of
366 geology and precipitation. All geology is found within 60 km of the chasm edge, but the
367 *e*-folding distance of the cumulative precipitation is significantly larger, 70-110 km. ~95%
368 of snow is found within 250 km of the chasm edge.

369 All these metrics show that the area of precipitation is more extensive than the mapped
370 area of channel networks. Extensive erosion has occurred and mapping efforts are incom-
371 plete, so this may be an artifact of incomplete preservation and high-resolution imaging.
372 For example, there is a 25km-diameter ejecta blanket in our area of highest modeled pre-
373 cipitation that may be obscuring underlying channels. If precipitation is necessary to form
374 or indurate plateau layered deposits, decline in the precipitation at 100-200 km from the
375 chasm (Figure 11) will create thin, or weakly-indurated deposits. These could easily be
376 missed during mapping, removed by the wind, or both. It is possible that the relatively
377 low horizontal resolution of our simulations is artificially broadening our modeled precip-
378 itation. Alternatively, there may be a threshold precipitation level to produce layered
379 deposits and channels. For example, sublimation losses may occur during the months
380 between deposition and the beginning of the melt season. These sublimation losses are
381 not included in our simulations, and will thin the snowpack everywhere while reducing

382 the area of remaining snow. Sediment mobilization is very sensitive to small changes in
 383 runoff:

$$Q_{sed} \propto (\tau_b - \tau_{crit})^{3/2} \quad (5)$$

384 where Q_{sed} is sediment flux, $\tau_b \propto H$ is bed shear stress and is proportional to flow depth
 385 H , and τ_{crit} is critical bed shear stress. If snow availability is a limiting factor, this will
 386 focus channel incision on areas with high precipitation rates.

5. Will snow melt?

387 We use a simple probabilistic melting model, described in Paper 1, to determine the
 388 likelihood of melting for the range of orbital conditions possible on pre-modern Mars.
 389 Our model is probabilistic because the true orbital parameters are not known for ages
 390 $\gg 10$ Mya [Laskar *et al.*, 2004]. This model tracks energy flow in snowpack as a balance
 391 of radiation, conduction, and evaporative cooling. A constant downgoing longwave flux
 392 from the atmosphere of 55 W/m^2 is assumed. This is approximately the peak afternoon,
 393 equatorial, perihelion greenhouse effect in low-dust conditions on contemporary Mars
 394 [Lewis *et al.*, 1999; Millour *et al.*, 2008], and a constant longwave flux at this value is
 395 found to correctly reproduce the effect of the atmosphere on annual peak temperature
 396 on contemporary Mars (Paper 1). The probability of melting Mars snowpack depends
 397 on surface albedo, snowpack thickness, latitude, solar luminosity, orbital conditions, and
 398 the atmospheric state. The Juventae channels are at 4°S , and all our calculations are
 399 for the equator. We assume a pressure of 1220 Pa, and so we ignore transfer of sensible
 400 heat from the surface to the atmosphere. Hecht [2002] shows that sensible heat losses are

401 more than 10 times smaller than evaporative cooling for this low pressure. As in Paper
402 1, we assume 70% humidity, which is optimistic in terms of melting because it reduces
403 evaporative cooling by $\approx 31\%$ relative to the zero-humidity case.

404 The probability of melting depends on snow albedo, which is high for pure snow but
405 much lower for realistic, dust-contaminated snow. *Warren & Wiscombe* [1980] show that
406 1000 ppmw dust can reduce ice albedo from >0.9 to 0.3. In the words of *Langevin et*
407 *al.* [2005], “Water ice is very bright in the visible spectrum when clean, but even a small
408 amount of dust contamination can reduce the albedo to values close to that of the dust
409 itself if the dust grains are embedded in ice grains.” *Clow* [1987] shows that 1000 ppmw
410 dust reduces snow albedo to 0.45-0.6 for grain sizes $400\mu\text{m}$ - $100\mu\text{m}$, respectively. This
411 is for precipitation grain sizes in our model; metamorphism will increase grain size and
412 decrease albedo. The mean bolometric albedo of bright regions in Mars’ North Polar
413 Residual Cap is inferred to be 0.41 from energy balance [*Kieffer et al.*, 1976]. Near-
414 infrared spectroscopy has identified seasonal water ice layers up to 0.2 mm thick on pole-
415 facing slopes in the Mars low latitudes [*Vincendon et al.*, 2010]. Analysis of the spatial
416 and seasonal dependence of these detections indicates that low-latitude surface water ice
417 has albedo 0.3 – 0.4 [*Vincendon et al.*, 2010]. Modelling of OMEGA data indicates that
418 water-rich terrains in the South Polar Layered Deposits have albedo $\sim 0.3 - 0.4$ (Figure
419 7 in *Douté et al.* [2007]). Measurements of the gray ring component of Dark Dune Spots
420 in Richardson Crater at 72°S show it to be composed of seasonal water ice deposits with
421 an albedo of 0.25 – 0.30 [*Kereszturi et al.*, 2011]. When melting starts, the albedo of
422 dust-contaminated ice remains low because “when snow melts, the impurities often tend
423 to collect at the surface rather than washing away with the meltwater” [*Warren*, 1984],

424 forming a lag. Water has a low albedo, so stream and melt pond albedo is lower than
 425 unmelted surface albedo. *Gardner & Sharp* [2010] show that 2 ppmw soot can greatly
 426 reduce snow albedo. Soot is $200 \times$ more optically effective than Earth crustal dust, and
 427 presumably more effective than Mars dust. We model albedos from 0.28 (the albedo of
 428 Mars' dust continents; *Mellon et al.* [2000]) to 0.4.

429 The melting is also sensitive to orbital conditions. For example, at the equator, high
 430 eccentricity is more favorable for melting than is low eccentricity.

431 Our preferred melting scenario is melting of snowpack on the plateau during or shortly
 432 after the lake storm (although it is also possible that snowpack persists for multiple
 433 years, and a separate transient warming event occurs). We assume that the snowpack
 434 persists until the next melting season. Low-latitude sublimation rates modeled by GCM
 435 [*Madeleine et al.*, 2009] suggest this requires snowpack thicknesses >0.25 m w.e. Lakes
 436 with lifetime $>10^2$ hours generate this snowpack, given our modeled precipitation rates.
 437 Annual maximum temperatures are then the metric relevant to melting. With these
 438 assumptions, the melting probabilities for equatorial snowpack are those shown in Figure
 439 14. The left panel is for melting if the storm does not continue through the melt season,
 440 and the right panel is for melting if the storm does continue through the melt season.

441 Once liquid water is flowing, several feedbacks can extend its lifetime. In Greenland,
 442 supraglacial channels with water depth >0.5 m reduce the albedo to close to that of water
 443 (~ 0.05) [*Lüthje et al.*, 2006]. Viscous dissipation can balance evaporative cooling only if

$$S > \frac{eL}{\rho g u D} \quad (6)$$

444 where S is river slope, $e \sim 1$ mm/hr is evaporation rate, L is the latent heat of vaporization,
445 $\rho = 1000$ kg/m³ is density, g is Mars gravity, $u = O(1)$ m/s is stream velocity, and $D =$
446 $O(1)$ m is stream depth [Clow, 1994]. This condition is not satisfied for the Juventae
447 plateau channel networks (which have slopes $<1\%$; Table 4), so the stream will be roofed
448 over by ice. Insulation of streams by ice can greatly extend liquid water lifetime [Clow,
449 1987].

450 For the purpose of generating runoff, there is an optimum thickness of porous snowpack
451 that scales as the diurnal thermal skin depth. If the porous layer is deeper than the
452 diurnal thermal skin depth, melt percolating from the surface will refreeze.

6. Discussion of channel and layered deposit formation

453 In this section, we evaluate formation mechanisms for the layered deposits and interbed-
454 ded channel networks. First we review constraints, including measurements from our own
455 DTMs. We consider a series of options for the channel-forming mechanism, and test them
456 against these constraints. These different mechanisms all assume that water is sourced
457 from ephemeral lakes as in §2 - §5 (bottom row in Figure 3). Next we drop the assump-
458 tion that water is sourced from ephemeral lakes, and describe entirely different geological
459 scenarios (top row in Figure 3). We do not find decisive evidence that allows us to choose
460 between these channel forming mechanisms or geological scenarios, and so are left with
461 multiple working hypotheses. We conclude the section with a list of future tests that
462 could help decide among these multiple working hypotheses.

463 In agreement with previous work [Mangold *et al.*, 2008; Weitz *et al.*, 2008], we inter-
464 pret the networks of sinuous ridges and troughs to be fossil fluvial channels (Figure 15).
465 Juventae plateau channels have low to moderate sinuosity and we have only found 2-3

466 highly sinuous (meandering) channels. This should be compared to Gale-Aeolis-Zephyria,
467 where most channels meander [Burr *et al.*, 2009]. Most channels run down the present-day
468 0.2° NNE regional slope [Mangold *et al.*, 2008]. Sinuous ridge width distribution appears
469 bimodal. We suspect that the broader $O(10^2\text{m})$ sinuous ridges are inverted valleys. The
470 sinuous ridges are probably not eskers. Single channels transition between positive relief
471 and negative relief. The sinuous ridges show horizontal layering, are flat topped, locally
472 highly sinuous and reveal no coarse grains at HiRISE scale. These attributes do not
473 resemble Earth eskers, nor Mars eskers in southern Argyre Planitia [Banks *et al.*, 2009].

474 Given that the channel networks are fossil fluvial channels, endmember channel-forming
475 mechanisms are thermal erosion into ice, and mechanical erosion of sediment. These have
476 corollary implications for the composition of the light-toned layered deposits: in the ther-
477 mal erosion endmember case, the present-day plateau layered deposits contain significant
478 relict ice. An example on Earth of this endmember case is the snowmelt-fed channel
479 network that forms each summer on the Greenland ice sheet. In the mechanical erosion
480 endmember case, the present-day plateau layered deposits are composed of (indurated)
481 sediment grains. We seek to understand whether the observations favor one or the other
482 endmember mechanism.

6.1. Implications of constraints for channel-forming mechanisms

483 Many of the channels are preserved in inverted relief: On Earth channels can become in-
484 verted through cementation of channel fill, armoring by coarse grains of the channel floor
485 against erosion, or infilling of the channel by an erosionally resistant material such as
486 lava [Williams *et al.*, 2009]. We do not know how the Juventae plateau channel networks
487 became inverted, but careful study of similar channels elsewhere suggests increased ce-

488 mentation of the channel thread, followed by differential erosion, as the most likely cause
489 [*Williams et al.*, 2009; *Burr et al.*, 2010]. The inverted channels lack evidence (such as
490 pitting) for sublimation . They are often horizontally or subhorizontally layered, and the
491 layers have variations in tone. They have well-defined, smooth, flat tops. These observa-
492 tions suggest that the inverted channels are composed of sediment and are not ice-cored.
493 Sediment fill is more consistent with the mechanical erosion endmember scenario than the
494 thermal erosion endmember scenario.

495 However, inverted channels on Mars do occur in ice-dominated, supraglacial and
496 proglacial settings. Midlatitude Amazonian glacier-associated channels at Lyot Crater
497 (HiRISE image ESP_016339_2225), Acheron Fossae (HiWish image ESP_018178_2165),
498 and E of Reull Valles (HiWish image ESP_020055_1410) have become inverted [*Fassett et*
499 *al.*, 2010]. The Acheron inverted channel is ≤ 80 Ma based on the age of its source glacier
500 [*Fassett et al.*, 2010]. In each cases, the glacier-associated channels appear to have incised
501 into ice, but to have been incompletely filled with debris and sediment during or after
502 incision. As the surrounding ice retreats due to sublimation, the channel-filling sediment
503 is left as a sinuous ridge. Therefore, the interpretation that the inverted channels are
504 composed of (indurated or cemented) sediment fill does not rule out the thermal erosion
505 endmember scenario.

506 The layered deposits are tens of meters thick: The present-day thickness of the plateau
507 layered deposits close to the chasm edge is 43 ± 11 m ($n = 13$), measured from HiRISE
508 DTMs. 33-39 layers are visible in HiRISE images of the thickest exposures (defining layers
509 using laterally continuous changes in tone, slope or erosional morphology).

510 In the thermal erosion endmember scenario in Figure 3, the layered deposits are pri-
511 marily water ice. The deposit thickness of $44\pm 13\text{m}$ then requires a minimum of 1400-2600
512 sols to accumulate at our peak precipitation of 0.9 mm/hr, ignoring sublimation losses.
513 The peak discharge of Maja Valles is $1.06 \times 10^8 \text{ m}^3\text{s}^{-1}$ [Kleinhans, 2005]. The volume
514 of Juventae Chasma below the pour point is $\sim 7 \times 10^4 \text{ km}^3$ (ignoring the volume of Maja
515 Valles itself). If this missing volume is 70% rock by volume and was exported over the
516 spillway, then with a fluvial sediment concentration of 1% by volume, the minimum cu-
517 mulative time to carve Maja Valles is 740 sols. Peak discharge exceeds mean discharge, so
518 Maja Valles operated for longer than this calculation suggests. In addition, an unfrozen
519 lake may have remained in Juventae after the end of channel formation. Making the
520 conservative assumption that there is only open water at the lake surface only when a
521 catastrophic flood is occurring, the predicted deposit thickness is 28%-53% of the observed
522 thickness. Because this is a lower limit, we do not think this discrepancy rules out the
523 thermal erosion endmember scenario.

524 The thickness of the deposits is harder to explain in the mechanical erosion endmember
525 scenario (Figure 3), in which the present-day plateau deposits are (indurated) sediments.
526 Enough atmospherically-transported material (sand, dust, and volcanoclastic material)
527 must be brought in from other regions of a primarily dry Mars to account for observed
528 thicknesses. For realistic cumulative outflow channel activity durations, not enough at-
529 mospheric dust flows into the storm zone *during the storm events* to precipitate as ice
530 nuclei and account for observed thicknesses. It is not possible for the layered deposits
531 to predate the channel-forming events, because channels at different levels within the de-
532 posit crosscut each other. Instead, the sediment would have to accumulate on the plateau

533 between storm events as sand, dust or volcanoclastic materials, or (less likely) be supplied
534 from the chasm floor during the early stages of outflow events by buoyant plumes. In
535 this case, the lake storms would be responsible for the channels, but would not be the
536 source of the material making up the layers. However, fluid released during snow melting
537 could be responsible for the induration or cementation of these materials, and thus their
538 long-term preservation (Figure 3).

539 Drainage density is up to 15 km^{-1} : Drainage density (units m^{-1}) is the sum of the channel
540 lengths within a region of interest, divided by the area of that region. Impact ejecta
541 locally armors the layered deposits against aeolian stripping, forming pedestal craters.
542 The highest drainage density that we have observed, 15 km^{-1} , is in the retreating margin
543 of one of these ejecta blankets (Figure 15 shows context, Figure 16a shows detail). Since
544 erosion by the wind preferentially removes finer channels, it is possible that this maximum
545 preserved value is representative of the original drainage density.

546 The drainage density observation is entirely consistent with the thermal erosion end-
547 member channel-forming scenario (Figure 3): supraglacial channels on the Greenland ice
548 sheet today have comparable drainage densities (e.g., 29 km^{-1} in the typical case shown
549 in Figure 16b).

550 The mechanical erosion endmember case is harder to reconcile with high drainage den-
551 sities, given that our model predicts low rates of snowfall and snowmelt. On Earth, high
552 drainage densities are found on steep topography (e.g., hillslopes in badlands) and in
553 areas subject to rare, intense rainstorms. Neither of these factors is likely to have been
554 present on the Juventae plateau, which has channels slopes typically $<1^\circ$. Several factors
555 could mitigate the difficulty of producing high drainage densities from mechanical ero-

556 sion driven by snowmelt on the Juventae plateau. Ground ice is stable at Juventae for
557 obliquities $>32^\circ$ [Mellon & Jakosky, 1995], which occur about $\frac{2}{3}$ of the time [Laskar et al.,
558 2004]. Using the same modelling approach that correctly predicted ground ice depth at
559 the Phoenix landing site [Mellon et al., 2009], ground ice at Juventae is predicted to form
560 an impermeable layer at 10^{-2}m - 10^{-1}m depth within the soil [Mellon & Jakosky, 1995].
561 A shallow impermeable layer would favor runoff over infiltration, so for a given afternoon
562 melt rate, would produce higher peak discharges. These would lead to a higher drainage
563 density than in the absence of a shallow impermeable layer. Assuming dry conditions be-
564 tween storm events, the sediment above any ice table is unlikely to have much inter-grain
565 cohesion. This would make it easier for runoff and shallow groundwater flow to dislodge
566 sediment grains from the channel head, lengthening the channel network and increasing
567 drainage density.

568 High drainage density is also entirely consistent with rainfall. The difficulty of raising
569 the atmosphere's temperature high enough to allow rainfall [Wordsworth et al., 2010a;
570 Wordsworth, 2010b] deters us from invoking rainfall so long as a snowmelt alternative is
571 possible.

572 Drainage basin and channel dimensions and slopes: Even if the channels were cut by ther-
573 mal erosion, some of them must have been infilled by sediment in order to form inverted
574 channels (Figure 3). If the channels are formed in fine sediment by mechanical erosion,
575 then sediment transport is required to form both the positive and the negative-relief
576 channels. Therefore, in either endmember case, sediment must be transported through
577 the observed channel network. The critical runoff R needed to initiate sediment transport
578 in a preexisting channel is [Perron et al., 2006]:

$$R_{crit} = \frac{1}{A} \frac{w^2 \rho' \tau_c^* D}{wS - 2\rho' \tau_c^* D} \left(\frac{8\rho' g \tau_c^* D}{f} \right)^{\frac{1}{2}} \quad (7)$$

579 where R_{crit} is the critical runoff rate, A is drainage area, w is channel width, $\rho' =$
 580 $(\rho_s/\rho_f) - 1$ is the normalized density, ρ_s is sediment density, ρ_f is fluid density, $\tau_c^* \approx 0.05$
 581 is the critical Shields number, D is sediment grain diameter, S is slope, g is Mars gravity, f
 582 is the Darcy-Weisbach friction factor, and all units are mks. We assume basaltic sediment
 583 $\rho_s = 3000 \text{ kg/m}^3$ and water density $\rho_f = 1000 \text{ kg/m}^3$. In alluvial streams, f is closely
 584 related to grain size, but no similar relationship has been published for thermally-eroded
 585 channels. A , w , and S are taken from our DTMs, as shown in Figure 17, tabulated in
 586 Table 4, and described below. *Area:* Erosion has scoured the deposits between preserved
 587 inverted channels, removing the drainage basins that once sourced those channels. We are
 588 therefore forced to divide the area between channels by equidistance. Because there have
 589 been multiple episodes of crosscutting flow, some truncation of channels by subsequent
 590 generations of channel may have occurred, which may lead to a systematic underestimate
 591 of A and corresponding overestimate of R_{crit} . *Width:* We measure channel widths using
 592 the distinctive, light-toned region at the top of the sinuous ridges visible in HiRISE images.
 593 DTMs confirm that this light-toned strip forms the summit of the much broader ridge, and
 594 often resolve a break-in slope near the top of the ridge approximately corresponding to the
 595 light-toned strip in the red-filter HiRISE images. By analogy with inverted channels near
 596 Green River, Utah [Williams et al, 2007], these observations suggest that the bright region
 597 whose width we are measuring corresponds to an erosionally resistant and vertically thin
 598 channel-fill deposit capping underlying weaker material. The channel widths we obtain
 599 are several meters for drainage areas $O(1) \text{ km}^2$ (Table 4). These widths may correspond to

600 indurated channel fill (or valley fill) sediments that are wider than was the instantaneous
601 channel. *Slope:* We take an average slope along the exposed length of the channel. There is
602 no visually obvious evidence of major postdepositional tilting of the plateau - the channels
603 run approximately down the present-day slope. We do not understand why the channels
604 frequently run parallel to each other before confluence.

605 R_{crit} for a catchment of area 1.6 km^2 and slope 0.8° feeding a channel of width 3.3m
606 is shown in Figure 18. (The adjacent catchment of area 2.1 km^2 produced almost indis-
607 tinguishable results). Both networks are from DTM1 (Appendix B). We assume $R \approx M$,
608 where M is the melt rate. This is a reasonable approximation if background climate con-
609 ditions are subfreezing and there is a shallow impermeable ice table, or if the substrate
610 is covered with fine-grained material that has a low infiltration rate. An upper limit on
611 M is if all precipitation melts upon reaching the ground. Then the resulting runoff can
612 mobilize coarse gravel (thick black line in Figure 18). However, a more realistic melt rate
613 is 0.1 mm/hr . This is still capable of initiating the transport of coarse sand and fine
614 gravel through the network (lower bound of gray envelope in Figure 18). The upper limit
615 on the gray envelope in is an order-of-magnitude error intended to capture errors in the
616 precipitation model, weather, and especially the width and area measurements discussed
617 above. We conclude from the area covered by this gray envelope that if boulder-sized
618 ($>256 \text{ mm}$ diameter) clasts have been transported through these Juventae channel net-
619 works, that would be strong evidence against localized precipitation. *Howard et al.* [2007]
620 provides criteria for distinguishing fluvially-transported boulders from postdepositionally
621 cemented blocks. Any clast that can be resolved by HiRISE is a boulder.

622 Pitted upper surfaces: The plateau layered deposits have pitted upper surfaces. Pits are
623 elongated approximately parallel to the present-day prevailing wind. *Le Deit et al.* [2010]
624 interpret some of these irregular depressions as sublimation pits. If correct, this would
625 imply that the layered plateau deposits contain relict ice. It is unclear from HiRISE
626 images (e.g., PSP_008853_1760) whether these are in fact sublimation features. Because
627 Juventae is equatorial, the usual criterion employed for recognizing sublimation features
628 in the midlatitudes – north/south slope asymmetry – cannot be used.

6.2. Alternative interpretations and tests

629 In §2, we inferred that location adjacent to a chasm must supply one or more limiting
630 factors for inverted channel formation, and that likely limiting factors included availability
631 of snow or rain, sufficient heat for melting, availability of mobilizable sediments, cementing
632 fluids, and incomplete erosion. In §3 - §5, we developed and tested the hypothesis that
633 precipitation is limiting. The results are consistent with the hypothesis. What about
634 heat, sediment, cementing fluids, and erosion? Can we rule any or all out?

635 Precipitation on the Valles Marineris plateau sourced from ephemeral chaos lakes is one
636 parsimonious model compatible with the current data, but other scenarios are possible
637 (Figure 3). For example, we cannot currently rule out a scenario where the observed
638 narrow, extended Valles Marineris cloud trails (0.4 micron effective diameter; *Clancy et*
639 *al.* [2009]) increase spectacularly in mean grain size and move closer to the canyon edge
640 during different orbital conditions or dust loading, permitting regional precipitation. Near-
641 surface water-ice morning fog occurs in Valles Marineris today [*Möhlmann et al.*, 2009],
642 and OMEGA has detected surface water ice on the northern wall of Coprates Chasma
643 [*Vincendon et al.*, 2010]. Net annual ice accumulation within the Valles Marineris occurs

644 in GCMs at high and moderate obliquity [*Madeleine et al.*, 2009], although this is largely
645 due to the high thermal inertia of the chasm walls (J.B. Madeleine, via email). Taken
646 together, this evidence suggests that Valles Marineris is a preferred site for equatorial
647 ice precipitation, which is important at high obliquity [*Mischna et al.*, 2003; *Forget et al.*,
648 2006]. In this scenario, snowpack is broadly distributed in the Valles Marineris region, but
649 generally does not melt. This possibility is discussed by *Le Deit et al.* [2010]. The limiting
650 factor provided by the chaos regions is then airborne darkening agents (ash and/or debris)
651 lofted by buoyant plumes (“dirty thunderstorms”; *van Eaton et al.* [2010]), which lead
652 to patchy melting or patchy preservation of a broadly distributed, preexisting snowpack.
653 Alternatively, the ash and/or debris forms a cast of the channels, which form over a broad
654 region but disappear elsewhere when the snowpack sublimates. A weakness of this scenario
655 is that both the observed fog and surface ice, and the predicted high-obliquity net ice
656 accumulation, are on the chasm floor and walls rather than the adjacent plateau. Figure
657 2 shows that opal-bearing layered deposits and channel networks are overwhelmingly found
658 on the plateau, not the floor and walls.

659 Another alternative source of water is springs, before chasm opening had begun.
660 Spillover of blister auefis, or groundwater, could source springs [*Gaidos & Marion*, 2003;
661 *Murchie et al.*, 2009b]. In this scenario, the layers and channel networks predate outflow
662 channel formation. This would not explain the downwind preference for channel networks,
663 but there is a 7% possibility that this could be due to chance (§4, Figure 12).

664 Among these three scenarios, our preference for the late formation model is tentative,
665 but testable. First, a more complete study of the channel networks, using HiRISE DTMs
666 where possible, and using channel width as a proxy for discharge (*Montgomery & Gran*

[2001] and references therein), would test the spring hypothesis and the precipitation hypotheses. If the channels were fed by a small number of point or line sources, channel widths should be constant between confluences (and channel sources should correlate to linear fractures, shear bands, or mineralogical anomalies). If precipitation or distributed groundwater flow fed the channels, channel widths should increase with contributing area as seen on Earth, and channel sources should not be correlated with fractures or mineralogical anomalies. Second, further tests of the localized-precipitation model at sites including Ganges Chasma, Cerberus Fossae and Mangala Fossae might uncover inconsistencies that would weaken the model's application at all sites including Juventae. We report initial results from one such test (at Echus) in §7.

Additional predictions are specific to the thermal-erosion endmember scenario (Figure 3): failure of these predictions would not rule out the mechanical-erosion endmember scenario (Figure 3). The thickness of the layered deposits should decrease away from the chasm edge in proportion to the mean precipitation rates predicted by localized precipitation models (e.g., Figure 9). Finally, SHARAD observations can test if the light-toned layered deposits have a dielectric constant consistent with ice, as is required by the thermal-erosion endmember scenario. SHARAD has a free-space wavelength of 15m, so the light toned layered deposits are thick enough for this test.

We do not understand the cause of the opal and hydrated-ferric-sulfate mineralization of parts of the Juventae plateau layered deposits. In the K'au desert downwind of the active Kilauea caldera on Hawaii's Big Island, opal and jarosite depositional coatings accumulate with minimal liquid water [*Schiffman et al.*, 2006; *Chemtob et al.*, 2010]. This Earth analog may not be directly applicable to Valles Marineris, because at Kilauea opal mineralization

690 is not found more than a few kilometers from the volcanic vents, in contrast to the more
691 extensive areas of opal mineralization on the Valles Marineris plateau [*Chemtob et al.*,
692 2010]. Because of the quantities involved, the presence of inverted channels appears to
693 set a more stringent lower limit on liquid water availability on the plateau than does the
694 opal and hydrated-ferric-sulfate mineralization.

7. Echus plateau

695 The greatest of the outflow channels is Kasei Valles [*Williams et al.*, 2000]. Kasei's source
696 is lava-floored Echus Chasma. Beyond the 5km-high chasm wall, on the Hesperian plateau,
697 dendritic channel networks are abundant (Figure 19a, *Chapman et al.* [2010a, b][*Mangold*
698 *et al.*, 2004, 2008]. The floor of Echus Chasma is now 200m below a saddle that marks
699 the start of the main channel. Regional topography suggests that the floor of Echus was
700 once much deeper [*Harrison & Chapman*, 2008].

701 Although no opal or hydroxylated sulfates have been reported on the Echus plateau
702 [*Milliken et al.*, 2008], the erosional properties of the substrate for the Echus channel
703 networks resembles the erosional properties of the Juventae plateau layered deposits.
704 Material on the SE rim of Echus is relatively thinly layered, relatively light-toned in
705 outcrop, and recessed from the chasm edge, suggesting a sedimentary or volcanoclas-
706 tic origin (CTX image P14_006586_1800_XN_00N079W). It is cut by very broad valleys,
707 which bottom out on more resistant basalt, suggesting it is less resistant to fluvial erosion
708 (P02_001839_1806_XN_00N079W).

709 Our simulations of the Echus plateau channel networks, which are preserved in negative
710 relief, show peak non-lake precipitation in the densest area of observed channels, at 0.7
711 mm/hr (Figure 19a). Because of the interaction of lake convergence, topography, and the

712 regional windfield, precipitation is also predicted S and E of the chasm beyond the existing
713 mapped area of channels. THEMIS and CTX show extensive channelization in these areas
714 (dotted lines in Figure 19a), which die away on a length scale similar to the length scale
715 of predicted precipitation (Figure 19b). cursory inspection of CTX images further away
716 from the channel edge does not show channelization. These results are consistent with
717 localized precipitation.

718 The Echus plateau channel networks are deep and extensive. *Chapman et al.* [2010b]
719 gives 82 km^3 total erosion over an eroded outcrop of $\sim 30000 \text{ km}^2$, corresponding to an
720 average of 2.7m material removed. With a melt season length of 30 sols and melting of 1
721 mm/day, this would require 90 years to remove if the material was primarily ice. However,
722 if the material is non-ice with a fluvial sediment:water ratio of 100:1, 9000 years would be
723 required to cut the observed channels.

724 Although the relatively incomplete geomorphic mapping of the Echus headwaters cur-
725 rently prevents more thorough hypothesis testing, this is a promising initial result that
726 suggests our ability to match observations at Juventae with only localized precipitation
727 can be reproduced elsewhere.

8. Implications for regional and global climate change

728 The majority of water vapor released in our simulations is trapped by localized precipita-
729 tion near the lake, and so is unavailable for broader climate change (Figure 13). Because
730 the remaining atmospheric vapor load is less than present-day global loads [*Smith*, 2002],
731 we do not expect a global excursion to wet conditions (the MEGAOUTFLO hypothesis;
732 *Baker et al.* [1991]; *Baker* [2001]; *Quantin et al.* [2005]) to result from water vapor release
733 during chaos events (Fig 13). There are four possible caveats. First, simultaneous trig-

gering of chaos events in multiple chasms, or the broad area of outwash at the terminus
of the outflow channels, would provide a larger interface for water vapor injection to the
atmosphere than is simulated here. Supposing an evaporation rate of 2 mm/hr, for 5%
global water cover, and in the absence of precipitation, the atmosphere will contain 6
mbar water in 70 sols. Water vapor is a powerful greenhouse gas and 6 mbar of water
vapor would cause noticeable global warming. But precipitation will occur, and it is likely
that outwash freezes over in $\ll 70$ sols. In addition, higher-resolution images have shown
inner channels within the outflow channels, indicating that much lower discharge rates,
and multiple flooding events, incised the outflow channels [Williams *et al.*, 2000]. This
does not support the hypothesis of large Late Hesperian and Amazonian seas, because at
low discharges, water would freeze and perhaps sublime, redepositing at planetary cold
traps. Second, noncondensable gases such as CO₂ or CH₄, stored in cryosphere clathrates
(or deep aquifers) and outgassed during chaos events [Bargery & Wilson, 2010], could
provide warming. Third, if chaos events are triggered by magma bodies laden with CO₂,
SO₂, and halogens, then chaos events and transient greenhouse warming could occur si-
multaneously (e.g., Johnson *et al.* [2008]). Fourth, if atmospheric pressure was higher
(e.g. hundreds of mbar) this would suppress the buoyant instability that leads to local-
ized precipitation (allowing more water vapor to escape to the background atmosphere;
Paper 1).

Our model indicates that regional or global temperatures warmer than today are not
required to explain the outflow-channel associated valley networks – the melting probabili-
ties for present-day solar luminosity are high (Figure 14). With DTM drainage network
and channel geometries, 0.1 mm/hr is approximately the required runoff for mobilization

757 of fine gravel/granules, and 1.0 mm/hr will mobilize medium gravel (Figure 18). Assum-
758 ing the albedo of dust, present-day solar luminosity, and the pdf of orbital parameters for
759 0.05 Gya, the probability of melting is 70% and the exceedance probability for melt rates
760 of 0.1 mm/hr is 30% (although melt rates of 1.0 mm/hr are not found). These percentages
761 are not precise, because of our crude treatment of the atmospheric contribution to surface
762 temperature.

763 However, our calculations indicate a greatly reduced melting probability for reduced
764 (3.0 Gya; Late Hesperian/Early Amazonian) solar luminosity, if the strength of the atmo-
765 spheric greenhouse was no greater than today (Figure 14). Taking into account the 6K
766 increase in afternoon temperature due to the water vapor released by the lake increases
767 the melting probability to 21%, and the melting exceedance probability to 8% for 0.1
768 mm/hr. However, this requires that the chaos lake starts in (or persists through) the melt
769 season. These are still low probabilities, so why are channels found throughout the strati-
770 graphic column? We suggest four possible explanations. (1) Melting is needed to produce
771 water that indurates the sediment. Since induration increases resistance to aeolian ero-
772 sion, the stratigraphic record on the Juventae plains is biased toward chaos storms that
773 were accompanied by melting. (2) Runoff accompanied only a few layer-forming events,
774 but the channels cut from the top to the bottom of the sedimentary stack. Meltwater
775 percolated through the stack and cemented all layers. Deeply-incising, rather than su-
776 perfcial, channels are suggested by the observation of negative-relief channel continuous
777 with channel-topped ridges (Figure 17). If the 33-39 layers identifiable in the stratigraphic
778 column correspond to 33-39 lake events, and modeling melt events as a Poisson process,
779 the probability of melting occurring on the plateau at some point in the year following at

780 least one chaos event is 12% - 14% for albedo = 0.28 for a greenhouse effect unchanged
781 from today. This increases to >99.9% if we assume a modest 6K increase in greenhouse
782 forcing. (3) The chaos events were correlated with orbital conditions, with chaos events
783 preferentially occurring during times that favored melt. (4) A greater past concentration
784 of greenhouse gases compensated for the faint young Sun, so that the background climate
785 state was warmer than in our calculations. This would lift the percentage of snowstorms
786 that would deposit ice which would melt.

787 Channel networks at SW Melas Chasma and Gale-Aeolis-Zephyria also formed in the
788 Late Hesperian or Amazonian, but because there is no conclusive evidence for groundwater
789 release at these locations it is difficult to make the case for localized precipitation. *Kite*
790 *et al.* [in prep.] propose a separate formation scenario for SW Melas Chasma and Gale-
791 Aeolis-Zephyria which requires unusual orbital conditions favoring snowmelt, but also does
792 not require a greenhouse effect stronger than the present day. Thermokarst at Ares Valles
793 has also been argued to require transient global warm conditions during the Hesperian
794 [*Warner et al.*, 2010].

795 The dendritic channels provide strong evidence for water runoff, so if the plateau layered
796 deposits record global conditions, then they would be *prima facie* evidence that temper-
797 atures and pressures permitting surface liquid water runoff persisted (or were revived)
798 well after the Late Noachian/Early Hesperian maximum in valley network formation.
799 However, we do not believe that they required globally-moist conditions.

9. Conclusions

800 We conclude from this study that:-

801 (1) Material lofted from Juventae Chasma and transported W by the background wind
802 field very likely contributed to channel formation on the Juventae plateau. This material
803 could be water or sediment or both;

804 (2) Peak precipitation over land occurs to the SW of the chasm in mesoscale simulations
805 of lake storms at Juventae Chasma. This corresponds to the location of the observed
806 plateau channel networks. The location is sensitive to lake surface elevation;

807 (3) Peak precipitation of 1.7 mm/hr water equivalent (w.e.) and mean rates of 0.9
808 mm/hr w.e. occur at the location of the observed plateau channel networks. These rates
809 are sensitive to lake surface elevation and lake temperature;

810 (4) Using present-day orbital conditions, 3.0 Gya solar luminosity, and the albedo of
811 dust leads to $O(10\%)$ probability of peak snowpack melting rate exceeding 0.1 mm/hr,
812 per event bed. This includes the greenhouse effect of vapor from the storm (or, equiva-
813 lently, a modest 6K increase in the background greenhouse effect). Neglecting infiltration
814 and evaporation losses, this discharge is sufficient to move sand and fine gravel through
815 the observed channels. The maximum observed drainage densities are consistent with
816 snowmelt channels thermally eroded into ice;

817 (5) The minimum background atmospheric temperature to permit surface melting is
818 sensitive to snowpack albedo, solar luminosity and orbital conditions;

819 (6) Juventae's plateau channel networks could have formed from localized precipitation,
820 and do not require global climate change;

821 (7) The majority of water vapor released to the atmosphere during chaos flooding is
822 trapped by localized precipitation at the chasm edge, and is not available to drive global
823 climate change;

824 (8) Alternative explanations of channel formation that are compatible with stratigraphic
825 constraints include patchy melting of broadly distributed equatorial snowpack, and spring
826 discharge of groundwater on the plateau early in the formation of Juventae Chasma;

827 (9) Our model strongly predicts that plateau channel networks will not be found >
828 250 km from a water vapor source. It also predicts that additional plateau channel
829 networks and plateau layered deposits should be identified downwind of large, localized
830 vapor sources elsewhere on Mars.

Appendix A: Methods

831 The fully compressible dynamical core of MRAMS is derived from the terrestrial RAMS
832 code [*Pielke et al.*, 1992]. A cloud microphysical scheme derived from CARMA was
833 recently added to MRAMS by T.I. Michaels. This cloud microphysics scheme has been
834 used to successfully reproduce observations of low-latitude clouds downwind of the Tharsis
835 Montes and Olympus Mons [*Michaels et al.*, 2006]. A recent description of MRAMS
836 capabilities is *Michaels & Rafkin* [2008b].

837 We made minimal modifications to the MRAMS v.2.5-01 code to allow for surface
838 liquid water. Liquid water microphysics is not included. Water vapor thermodynamics
839 are included in the energy equation, but water vapor is not included in the mass and
840 momentum equations – that is, we ignore pressure and virtual temperature effects of
841 water vapor loading.

842 We do not permit dynamic dust lifting at the mesoscale.

843 Model vertical layer thickness varied from 2.3 km at altitude to 30 m near the ground.
844 We used four grids with the outermost being hemispheric and a horizontal resolution of
845 ~ 8.9 km on the inmost grid. Output was sampled every 1/24 sol (≈ 3699 s), or ‘Mars-

hour.’ We assume that this frequency, limited by available disk space, is enough to capture
model behaviour – for example, we refer to the warmest of 24 samples during a sol as the
‘day’s maximum temperature.’ The timestep varied between runs but was never more
than 3.75s on the inmost grid.

Atmospheric boundary conditions are from the NASA Ames MGCM [*Haberle et al.*,
1993], v2.1, and we use present-day orbital parameters.

Appendix B: HiRISE stereo DTMs

HiRISE DTMs were generated using SOCET SET following USGS recommended procedure [*USGS*, 2009].

DTM1: Juventae1, PSP_003223_1755/PSP_003724_1755

DTM2: Juventae2, PSP_004423_1755/PSP_005412_1755

DTM3: Ganges1, PSP_005161_1720/ESP_016237_1720

All DTMs, together with the corresponding orthorectified HiRISE images, can be obtained for unrestricted further use from the lead author.

In addition, we made use of PDS released files for a Juventae plateau stereopair, PSP_003434_1755 / PSP_003579_1755.

Acknowledgments. HiRISE stereo DTMs were produced on the SOCET SET workstation at the SETI Institute, generously made available by Cynthia Phillips. Ross Beyer, Annie Howington-Kraus, Audrie Fennema, and Sarah Mattson assisted with DTM generation. We thank Teresa Segura for advice on starting the project, and Inez Fung, Rebecca Williams, Jean-Baptiste Madeleine, Max Rudolph and Leif Karlstrom for useful discussions. We thank Janice Bishop, Keith Harrison, and Bob Grimm for commenting

867 on the manuscript. Caleb Fassett drew our attention to inverted channels near Reull
868 Vallis. This work made use of Bin Guan's scripts. We are grateful to the HiRISE team
869 for maintaining a responsive public target request program (HiWish), that was useful for
870 this work. We acknowledge support from Teragrid allocation TG-EAR100023, NASA Sci-
871 ence Mission Directorate grant NNX08AN13G, NASA Science Mission Directorate grant
872 NNX09AN18G, and NASA grants to SwRI which funded cloud microphysics capabilities.

References

- 873 Andrews-Hanna, J.C., & R.J. Phillips (2007), Hydrological modeling of outflow channels
874 and chaos regions on Mars, *J. Geophys. Res.* 112, E08001, doi:10.1029/2006JE002881.
- 875 Baker, V.R., et al. (1991), Ancient oceans, ice sheets and the hydrological cycle on Mars,
876 *Nature* 352, 589-594.
- 877 Baker, V.R. (2001), Water and the martian landscape, *Nature* 412, 228-236,
878 doi:10.1038/35084172
- 879 Banks, M.E., et al. (2009), An analysis of sinuous ridges in the southern Argyre Planitia,
880 Mars using HiRISE and CTX images and MOLA data, *J. Geophys. Res.* 114(E9),
881 E09003, doi:10.1029/2008JE003244.
- 882 Bargery, A.S., & L. Wilson (2010), Dynamics of the ascent and eruption of water contain-
883 ing dissolved CO₂ on Mars, *J. Geophys. Res.* 115, E05008, doi:10.1029/2009JE003403.
- 884 Barnhart, C.J., A.D. Howard & J.M. Moore (2009), Long-term precipitation and late-stage
885 valley network formation: Landform simulations of Parana Basin, Mars, *J. Geophys.*
886 *Res. - Planets* 114, E01003, doi:10.1029/2008JE003122.

- 887 Bishop J.L., et al. (2009), Mineralogy of Juventae Chasma: Sulfates in the light-toned
888 mounds, mafic minerals in the bedrock, and hydrated silica and hydroxylated ferric
889 sulfate on the plateau, *J. Geophys. Res.*, 114, E00D09, doi:10.1029/2009JE003352.
- 890 Box, J.E., & K. Ski (2007), Remote sounding of Greenland supraglacial melt lakes: im-
891 plications for subglacial hydraulics, *J. Glaciol* 53, 257-265.
- 892 Burr, D.M., et al. (2009), Pervasive aqueous paleoflow features in the Aeolis/Zephyria
893 Plana region, Mars, *Icarus* 200, p. 52-76, doi:10.1016/j.icarus.2008.10.014.
- 894 Burr, D. M., R. M. E. Williams, K. D. Wendell, M. Chojnacki, & J. P. Emery
895 (2010), Inverted fluvial features in the Aeolis/Zephyria Plana region, Mars: For-
896 mation mechanism and initial paleodischarge estimates, *J. Geophys. Res. - Planets*,
897 doi:10.1029/2009JE003496.
- 898 Carr, M.H., & M.C. Malin (2000), Meter-scale characteristics of Martian channels and
899 valleys, *Icarus* 146, 366-386.
- 900 Carr, M.H., & J.W. Head (2003), Basal melting of snow on early Mars: A possible origin
901 of some valley networks, *Geophys. Res. Lett.* 30, 2245, doi:10.1029/2003GL018575.
- 902 Carr, M.H., & J.W. Head (2010), Geologic history of Mars, *Earth and Planetary Science*
903 *Letters* 294, 185-203.
- 904 Catling, D.C., et al. (2006), Light-toned layered deposits in Juventae Chasma, Mars,
905 *Icarus* 181, 26-51.
- 906 Chapman, M.G., et al. (2010a), Amazonian geologic history of the Echus Chasma and Ka-
907 sei Valles system on Mars: New data and interpretations, *Earth and Planetary Science*
908 *Letters*, Volume 294, 238-255.

- 909 Chapman, M.G., et al. (2010b), Noachian-Hesperian geologic history of the Echus Chasma
910 and Kasei Valles system on Mars: New data and interpretations, *Earth and Planetary*
911 *Science Letters*, Volume 294, 256-271.
- 912 Chemtob, S.M., et al. (2010), Silica coatings in the Ka'u Desert, Hawaii, a Mars analog
913 terrain: A micromorphological, spectral, chemical, and isotopic study, *J. Geophys. Res.*
914 115, E04001, doi:10.1029/2009JE003473.
- 915 Clancy, R.T. et al. (2009), Valles Marineris cloud trails, *J. Geophys. Res. - Planets* 114,
916 E11002, doi:10.1029/2008JE003323
- 917 Clow, G.D. (1987), Generation of liquid water on Mars through the melting of a dusty
918 snowpack, *Icarus* 72, 95-127.
- 919 Clow, G.D. (1994), Minimum Discharge Rates Required for Sustained Water Flow on the
920 Martian Surface, *Lunar and Planetary Science Conference 25*, p.275.
- 921 Coleman, N.M., & V.R. Baker (2007), Evidence that a paleolake overflowed the rim of
922 Juventae Chasma, Mars, *LPSC 38*, 1338.
- 923 Conway, S.J., M.P. Lamb, M.R. Balme, M.C. Towner & J.B. Murray (2010), Enhanced
924 runout and erosion by overland flow at low pressure and subfreezing conditions: exper-
925 iments and application to Mars, *Icarus*, in press.
- 926 Douté, S., et al. (2007), South Pole of Mars: Nature and composition of the icy terrains
927 from Mars Express OMEGA observations, *Planet. and Space Sci.* 55, 113-133.
- 928 Eichenlaub, V. (1979), *Weather and climate of the Great Lakes region*, University of Notre
929 Dame Press.
- 930 Edgett, K.S. (2005), The sedimentary rocks of Sinus Meridiani: Five key observations
931 from data acquired by the Mars Global Surveyor and Mars Odyssey orbiters, *Mars 1*,

- 932 5-58, doi:10.1555/mars.2005.0002
- 933 Fassett, C.I., & J.W. Head III (2008), Valley network-fed, open-basin lakes on Mars:
934 Distribution and implications for Noachian surface and subsurface hydrology, *Icarus*
935 198, 37–56.
- 936 Fassett, C.I., & J.W. Head III (2008), The timing of martian valley network activity:
937 Constraints from buffered crater counting, *Icarus* 195, 61–89.
- 938 Fassett, C.I., et al. (2010), Supraglacial and proglacial valleys on Amazonian Mars, *Icarus*
939 208, 86–100.
- 940 Forget, F., et al. (2006), Formation of Glaciers on Mars by Atmospheric Precipitation at
941 High Obliquity, *Science* 368, 311.
- 942 Gaidos E. & G. Marion (2003), Geological and geochemical legacy of a cold early Mars,
943 *J. Geophys. Res. - Planets* 108(E6), 5055, doi:10.1029/2002JE002000.
- 944 Gardner, A. S., & M. J. Sharp (2010), A review of snow and ice albedo and the develop-
945 ment of a new physically based broadband albedo parameterization, *J. Geophys. Res.*,
946 115, F01009, doi:10.1029/2009JF001444
- 947 Garrett, J.R. (1992), *The Atmospheric Boundary Layer* (Cambridge Atmospheric and
948 Space Science Series), Cambridge Univ. Press
- 949 Golombek, M.P., et al. (2006), Erosion rates at the Mars Exploration Rover land-
950 ing sites and long-term climate change on Mars, *J. Geophys. Res.* 111, E12S10,
951 doi:10.1029/2006JE002754.
- 952 Grotzinger, J., et al. (2006), Sedimentary textures formed by aqueous processes, Erebus
953 crater, Meridiani Planum, Mars, *Geology* 34(12), 1085-1088; doi:10.1130/G22985A.1

- 954 Haberle, R.M., et al. (1993), Mars atmospheric dynamics as simulated by the NASA Ames
955 General-Circulation Model. 1. The zonal-mean circulation. *J. Geophys. Res. - Planets*,
956 98, 3093-3123.
- 957 Harrison, K.P., & M.G. Chapman (2008), Evidence for ponding and catastrophic floods
958 in central Valles Marineris, Mars, *Icarus* 198, 351-364.
- 959 Harrison, K.P., & R.E. Grimm (2008), Multiple flooding events in Martian outflow chan-
960 nels, *J. Geophys. Res.* 113, E02002, doi:10.1029/2007JE002951.
- 961 Hartmann, W.K. (2005), Martian cratering 8: Isochron refinement and the chronology of
962 Mars, *Icarus*, 174, 294-320.
- 963 Halevy, I., M.T. Zuber, & D. Schrag (2007), A Sulfur Dioxide Climate Feedback on Early
964 Mars, *Science* 318, 1903-1907.
- 965 Hayward, R.K., et al. (2006), Mars Global Digital Dune Database: MC2-MC29, U.S.
966 Geological Survey Open-File Report 2007-1158, version 1.0
- 967 Hecht, M.H. (2002), Metastability of liquid water on Mars, *Icarus* 156, 373-386.
- 968 Howard, A. D.; Moore, J. M.; Irwin, R. P.; Dietrich, W. E. (2007), Boulder Transport
969 Across the Eberswalde Delta, Lunar and Planetary Science Conference 38, abstract no.
970 1168
- 971 Hynek, B.M., & R.J. Phillips (2003), New data reveal mature, integrated drainage systems
972 on Mars indicative of past precipitation, *Geology* 31, 757-760
- 973 Hynek, B. M., M. Beach, & M. R. T. Hoke (2010), Updated Global Map of Martian
974 Valley Networks and Implications for Climate and Hydrologic Processes, *J. Geophys.*
975 *Res.*, doi:10.1029/2009JE003548, in press.

- 976 Kereszturi, A., Vincendon, M., & F. Schmidt, 2011, Water ice in the dark dune spots of
977 Richardson crater on Mars, *Planetary and Space Science* 59(1), 26-42.
- 978 Kieffer, H.H., et al., 1976, Martian north pole summer temperatures - Dirty water ice,
979 *Science* 194, 1341-1344.
- 980 Kite, E.S., M. Manga & I. Halevy (in prep.), Snowmelt model of the formation and
981 distribution of sedimentary rocks on Mars: Thick atmosphere not required?
- 982 Kite, E.S., et al., in review, Localized precipitation and runoff on Mars, *J. Geophys. Res.*,
983 available on arXiv astro-ph:EP.
- 984 Kleinhans, M.G. (2005), Flow discharge and sediment transport models for estimating a
985 minimum timescale of hydrological activity and channel and delta formation on Mars,
986 *J. Geophys. Res.* 110, E12003, doi:10.1029/2005JE002521.
- 987 Komatsu, G., et al. (2009), Paleolakes, paleofloods, and depressions in Aurorae and Ophir
988 Plana, Mars: Connectivity of surface and subsurface hydrological systems, *Icarus* 201,
989 474-491
- 990 Kraal, E.R., et al. (2008a), Catalogue of large alluvial fans in martian impact craters,
991 *Icarus* 194(1), 101-110.
- 992 Kraal, E.R., M. van Dijk, G. Postma, & M.G. Kleinhans (2008b), Martian stepped-delta
993 formation by rapid water release, *Nature*, 451, 973-976, doi:10.1038/nature06615.
- 994 Kuiper, K.F., et al. (2008), Synchronizing rock clocks of Earth history, *Science* 320, 500-
995 504.
- 996 Johnson, S.S., Mischna, M.A., Grove, T.L., & M.T. Zuber (2008), Sulfur-induced green-
997 house warming on early Mars, *J. Geophys. Res.* 113, doi:10.1029/2007JE002962.

- 998 Laskar, J. et al. (2004), Long term evolution and chaotic diffusion of the insolation quan-
999 tities of Mars, *Icarus* 170, 343-364.
- 1000 Le Deit, L., et al. (2010), Morphology, stratigraphy, and mineralogical composition of a
1001 layered formation covering the plateaus around Valles Marineris, Mars: Implications for
1002 its geological history, *Icarus*.
- 1003 Langevin, Y., et al. (2005), Summer Evolution of the North Polar Cap of Mars as Observed
1004 by OMEGA/Mars Express, *Science* 307, 1581-1584.
- 1005 Le Deit, L., et al. (2010), Morphology, stratigraphy, and mineralogical composition of a
1006 layered formation covering the plateaus around Valles Marineris, Mars: Implications for
1007 its geological history, *Icarus*, in press.
- 1008 Lewis, K.W., et al. (2008), Quasi-periodic bedding in the sedimentary rock record of Mars,
1009 *Science* 322, 1532.
- 1010 Lewis, K.W., et al. (2010), Global significance of cyclic sedimentary deposits on Mars,
1011 *LPSC* 41, 2648.
- 1012 Lewis, S.R., et al. (1999), A climate database for Mars, *J. Geophys. Res. - Planets* 104,
1013 E10, 24177-24194.
- 1014 Lüthje, M., et al. (2006). Modelling the evolution of supraglacial lakes on the West Green-
1015 land ice-sheet margin, *Journal of Glaciology* 52(179)
- 1016 McLennan, S. M., & J.P. Grotzinger (2008), The sedimentary rock cycle of Mars, in
1017 Bell, J., ed. *The Martian Surface - Composition, Mineralogy, and Physical Properties*,
1018 Cambridge University Press.
- 1019 Madeleine, J.-B., et al. (2009) Amazonian northern mid-latitude glaciation on Mars: A
1020 proposed climate scenario, *Icarus* 203, 390-405

- 1021 Markowski, P., & Y. Richardson (2010), Mesoscale meteorology in midlatitudes, John
1022 Wiley & Sons.
- 1023 Malin & Edgett (2003), Evidence for persistent flow and aqueous sedimentation on early
1024 Mars, *Science*, 302, 1931-1934
- 1025 Malin, M.C., et al. (2010), An overview of the 1985-2006 Mars Orbiter Camera science
1026 investigation, *Mars* 5, 1-60, doi:10.1555/mars.2010.0001
- 1027 Mangold, N. ,et al. (2004), Evidence for Precipitation on Mars from Dendritic Valleys in
1028 the Valles Marineris Area, *Science* 305. 78 - 81 DOI:10.1126/science.1097549
- 1029 Mangold et al. (2008), Geomorphic study of fluvial landforms on the north-
1030 ern Valles Marineris plateau, Mars, *J. Geophys. Res. - Planets* 113, E08009,
1031 doi:10.1029/2007JE002985
- 1032 McKenzie, D., & F. Nimmo (1999), The generation of martian floods by the melting of
1033 ground ice above dykes, *Nature* 397, 231-233.
- 1034 Mellon, M.T., & B.M. Jakosky (1995), The distribution and behavior of Martian
1035 ground ice during past and present epochs, *J. Geophys. Res.* 100(E6), 11781-11799,
1036 doi:10.1029/95JE01027.
- 1037 Mellon, M.T., et al. (2000), High-Resolution Thermal Inertia Mapping from the Mars
1038 Global Surveyor Thermal Emission Spectrometer, *Icarus* 148, 437-455.
- 1039 Mellon, M.T., et al. (2009), Ground ice at the Phoenix Landing Site: Stability state and
1040 origin, *J. Geophys. Res.* 114(E00E07), doi:10.1029/2009JE003417
- 1041 Metz, J., et al. (2009), Sublacustrine depositional fans in southwest Melas Chasma, *J.*
1042 *Geophys. Res.* 114, E10002, doi:10.1029/2009JE003365.

- 1043 Michaels, T.I., A. Colaprete, & S.C.R. Rafkin, Significant vertical water trans-
1044 port by mountain-induced circulations on Mars, *Geophys. Res. Lett.* 33, L16201,
1045 doi:10.1029/2006GL026562.
- 1046 Michaels, T.I., & S.C.R. Rafkin (2008), MRAMS today - One example of current Mars
1047 mesoscale modeling capabilities, Third International Workshop on Mars Atmosphere:
1048 Modeling and Observations, Williamsburg, Virginia, 9116.
- 1049 Milliken, R.E., et al. (2008), Opaline silica in young deposits on Mars, *Geology* 36, 847850,
1050 doi: 10.1130/G24967A.1.
- 1051 Millour, E., F. Forget, & S.R. Lewis (2008), Mars Climate Database v4.3 Detailed Design
1052 Document, downloaded from <http://www-mars.lmd.jussieu.fr/>
- 1053 Mischna, M.A., et al. (2003), On the orbital forcing of Martian water and CO₂ cycles:
1054 A general circulation model study with simplified volatile schemes, *J. Geophys. Res. -*
1055 *Planets* 108(E6), doi:10.1029/2003JE002051.
- 1056 Möhlmann, D.T.F., et al (2009), Fog phenomena on Mars, *Planet. & Space Sci.* 57, 1987-
1057 1992.
- 1058 Montgomery, D.R., & K.B. Gran (2001), Downstream variations in the width of bedrock
1059 channels, *Water Resources Research* 37(6), 1841-1846.
- 1060 Murchie, S.L., et al. (2009a), A synthesis of Martian aqueous mineralogy after 1 Mars
1061 year of observations from the Mars Reconnaissance Orbiter, *J. Geophys. Res. - Planets*
1062 114, E00D06, doi:10.1029/2009JE003342
- 1063 Murchie, S.L., et al. (2009b), Evidence for the origin of layered deposits in Candor
1064 Chasma, Mars, from mineral composition and hydrologic modeling, *J. Geophys. Res. -*
1065 *Planets* 114, E00D06, doi:10.1029/2009JE003343

- 1066 Perron, J.T., M. Manga, & M.P. Lamb (2004), Permability, recharge, and runoff
1067 generation on Mars, First Workshop on Mars Valley Networks. Downloaded from
1068 www.gps.caltech.edu/~mpl/perronetal_valleynetworks.pdf on 31 Oct 2010.
- 1069 Perron, J.T., M.P. Lamb, C.D. Koven, I.Y. Fung, & E. Yager (2006), Valley for-
1070 mation and methane precipitation rates on Titan, *J. Geophys. Res.* 111, E11001,
1071 doi:10.1029/2005JE002602.
- 1072 Pielke, R.A. (2002), *Mesoscale meteorological modeling*, 2nd edition (Intl. Geophysics
1073 series vol 78), Academic Press.
- 1074 Pielke, R.A., et al. (1992), A comprehensive meteorological modeling system - RAMS,
1075 *Meteorol. & Atmos. Phys.* 49, 69-91.
- 1076 Pielke, R.A. & Y. Mahrer (1978), Verification analysis of University-of-Virginia 3-
1077 dimensional mesoscale model prediction over South Florida for 1 July 1973, *Monthly*
1078 *Weather Rev.* 106, 1568-1589.
- 1079 Postberg, F., S. Kempf, J. Schmidt, N. Brilliantov, A. Beinsen, B. Abel, U. Buck
1080 & R. Srama (2009), §2.2 of supplementary information to: Sodium salts in E-ring
1081 ice grains from an ocean below the surface of Enceladus, *Nature* 459, 1098-1101,
1082 doi:10.1038/nature08046.
- 1083 Quantin, C. et al. (2005), Fluvial and lacustrine activity on layered deposits in
1084 Melas Chasma, Valles Marineris, Mars, *J. Geophys. Res. - Planets*, 110, E12S19,
1085 doi:10.1029/2005JE002440.
- 1086 Rafkin, S. C. R., Haberle, R. M., and T. I. Michaels (2001), The Mars Regional At-
1087 mospheric Modeling System (MRAMS): Model description and selected simulations,
1088 *Icarus*, 151, 228-256.

- 1089 Rafkin, S. C. R. and T. I. Michaels (2003), Meteorological predictions for 2003
1090 Mars Exploration Rover high-priority landing sites. *J. Geophys. Res.*, 108 No.
1091 E12,10.1029/2002JE002027
- 1092 Roach, L.H. et al. (2010), Hydrated mineral stratigraphy of Ius Chasma, Valles Marineris,
1093 *Icarus* 206, 253-268.
- 1094 Scambos, T., Hulbe, C., & M. Fahnestock (2003), Climate-induced ice shelf disintegration
1095 in the Antarctic peninsula, *Antarct. Res. Ser.* 79, 7992.
- 1096 Schiffman, P. et al., (2006), Acid-fog deposition at Kilauea volcano: A possible mecha-
1097 nism for the formation of siliceous-sulfate rock coatings on Mars, *Geology* 34, 921924;
1098 doi:10.1130/G22620A.1.
- 1099 Segura, T.L., O.B. Toon, T. Colaprete & K. Zahnle (2002), Environmental Effects of
1100 Large Impacts on Mars, *Science* 298, 1977-1980.
- 1101 Segura, T.L., O.B. Toon, & T. Colaprete (2008), Modeling the environmental effects of
1102 moderate-sized impacts on Mars, 113, E11007, doi:10.1029/2008JE003147.
- 1103 Smith, M.D. (2002), The annual cycle of water vapor on Mars as observed by the Thermal
1104 Emission Spectrometer, *J. Geophys. Res.* 107, 5115, doi:10.1029/2001JE001522.
- 1105 Spiga, A., & F. Forget (2009), A new model to simulate the Martian mesoscale and
1106 microscale atmospheric circulation: Validation and first results, *J. Geophys Res.* 114,
1107 E02009.
- 1108 Toon, O.B., T. Segura & K. Zahnle (2010), The Formation of Martian River Valleys by
1109 Impacts, *Ann. Rev. Earth & Planet. Sci.* 38, 303-322.
- 1110 United States Geological Survey (2009), USGS Astrogeology Science Center Tuto-
1111 rial: Stereo Processing using HiRISE Stereo Imagery ISIS3 and SOCET SET,

- 1112 June 2009, downloaded from <http://webgis.wr.usgs.gov/pigwad/tutorials/socetset/>
1113 SocetSet4HiRISE.htm
- 1114 van Eaton, A., et al., 2010, Microphysical Controls on Ascent of Water-Rich Ash Clouds
1115 from Supereruptions, AGU Fall Meeting 2010, abstract # V13C-2375
- 1116 Vincendon, M., F. Forget, & J. Mustard (2010), Water ice at low to mid latitudes on
1117 Mars, *J. Geophys. Res.* 115, E10001, doi:10.1029/2010JE003584.
- 1118 Warren, S.G., & W.J. Wiscombe (1980), A Model for the Spectral Albedo of Snow. II:
1119 Snow Containing Atmospheric Aerosols, *J. Atmos. Sciences* 37: 2734-2745.
- 1120 Warner, N. et al. (2010), Hesperian equatorial thermokarst lakes in Ares Vallis as evidence
1121 for transient warm conditions on Mars, *Geology* 38, 71-74.
- 1122 Wang, C.-Y., M. Manga, & C. Wong (2005), Floods on Mars released from groundwater
1123 by impact, *Icarus* 175, 551555.
- 1124 Warren, S.G. (1984), Impurities in snow - Effects on albedo and snowmelt, *Ann. Glaciol*
1125 5, 177-179.
- 1126 Weitz, C.M. et al. (2008) Light-toned strata and inverted channels adjacent
1127 to Juventae and Ganges chasmata, Mars, *Geophys. Res. Lett.* 35, L19202,
1128 doi:10.1029/2008GL035317
- 1129 Weitz, C.M. et al. (2010) Mars Reconnaissance Orbiter observations of light-toned layered
1130 deposits and associated fluvial landforms on the plateaus adjacent to Valles Marineris,
1131 *Icarus* 205, 73-102
- 1132 Williams, R.M.E. (2007), Global spatial distribution of raised curvilinear features on Mars,
1133 LPSC 38, 1821.

- 1134 Williams, R.M.E., Chidsey, T.C., Jr., & Eby, D.E., (2007), Exhumed paleochannels in
1135 central Utah - analogs for raised curvilinear features on Mars, in Willis, G.C., Hylland,
1136 M.D., Clark, D.L., and Chidsey, T.C., Jr., editors, Central Utah - diverse geology of a
1137 dynamic landscape: Utah Geological Association Publication 36, Salt Lake City, Utah,
1138 220-235.
- 1139 Williams, R.M.E., M.C. Malin, & K.S. Edgett (2005), Remnants of the courses of fine-
1140 sclaes, precipitation-fed runoff streams preserved in the Martian rock record, LPSC 36,
1141 1173.
- 1142 Williams, R.M.E., & M.C. Malin (2008), Sub-kilometer fans in Mojave Crater, Mars,
1143 Icarus 198, 365-383, doi:10.1016/j.icarus.2008.07.013
- 1144 Williams, R.M.E., et al. (2000), Flow rates and duration within Kasei Valles, Mars: Im-
1145 plications for the formation of a Martian Ocean, Geophys. Res. Lett. 27, 1073–1076.
- 1146 Williams, R.M.E., et al. (2009), Evaluation of paleohydrologic models for terrestrial in-
1147 verted channels: Implications for application to martian sinuous ridges, Geomorphology
1148 107, 300-315.
- 1149 Wordsworth, R., F. Forget, & V. Eymet (2010a), Infra-red collision-induced and far-line
1150 absorption in dense CO₂ atmospheres, Icarus, doi:10.1016/j.icarus.2010.06.010, in press.
- 1151 Wordsworth, R., et al. (2010b) Investigating the early Martian climate through three-
1152 dimensional atmospheric modelling, Exoclimes: Exploring the diversity of planetary
1153 atmospheres, Exeter UK.

Table 1. List of runs with parameters.

Run	Full name	Lake level (m)	Lake temp. (K)	Lake area (km ²)	Description
<i>juventae_dry</i>	juventae_Mar.12.2010	–	–	–	V.M. topography, no lake
<i>juventae_high</i>	juventae_May.12.2010	+ 0 m	273.15	25800	At spillway
<i>juventae_med</i>	juventae_Mar.13.2010	-1000 m	278.15	19400	Almost fills chasm
<i>juventae_low</i>	juventae_Mar.14.2010	-3000 m	278.15	6400	In SE corner of chasm
<i>echus_low</i>	echus_Apr.5.2010	-900m	278.15	3600	Small equant lake
<i>echus_high</i>	echus_Mar.25.2010	-800m	273.15	17100	At spillway, elongated N.S.

Table 2. Evaporation rate and vapor fate (end of sol 5). Units are Mt (10⁶ metric tons).

Italicized *dry* runs are subtracted from the runs below them. See also Figure 13.

Run	Evap. rate (mm/hr)	Water in atm.	Total atm.(%)	Snow in lake	Snow beyond lake	Total snow (%)
<i>juventae_dry</i>	0	536	100%	0	0	0%
<i>juventae_low</i>	2.47	304	18%	251	1166	82%
<i>juventae_med</i>	2.82	536	10%	1356	3472	90%
<i>juventae_high</i>	1.88	571	12%	1505	2590	88%
<i>juventae_dry_sol_7</i>	0	520	100%	0	0	0%
<i>juventae_low_sol_7</i>	2.54	403	15%	387	1887	85%
<i>juventae_med_sol_7</i>	2.90	658	8%	2230	5393	92%

Table 3. Model skill using method of *Pielke & Mahrer* [1978]. The best-fitting model for each geological target is highlighted in bold. Italicized text corresponds to the original extent of layered deposits mapped by *Weitz et al.* [2010], and normal text is the value for *Le Deit et al.* [2010]. 1.0 mm/hr is not shown because there is only 1 pixel with this value

Precip. (mm/hr)	Skill					Coverage				
	0.02	0.2	0.4	0.6	0.8	0.02	0.2	0.4	0.6	0.8
juventae_low	11	0	0	0	0	0.040	0	0	0	0
	<i>11</i>	<i>0</i>	<i>0</i>	<i>0</i>	<i>0</i>	<i>0.009</i>	<i>0</i>	<i>0</i>	<i>0</i>	<i>0</i>
juventae_med	5	19	50	108	122	0.020	0.071	0.185	0.403	0.455
	<i>5</i>	<i>19</i>	<i>51</i>	<i>138</i>	<i>227</i>	<i>0.004</i>	<i>0.015</i>	<i>0.041</i>	<i>0.111</i>	<i>0.182</i>
juventae_high	6	33	120	229	269	0.022	0.122	0.446	0.853	1.000
	<i>6</i>	<i>33</i>	<i>136</i>	<i>293</i>	<i>498</i>	<i>0.005</i>	<i>0.026</i>	<i>0.109</i>	<i>0.235</i>	<i>0.400</i>

Table 4. Measurements relevant to hydrology for 2 adjacent inverted channels (Figure 17).

			Catchment 1	Catchment 2
<i>A</i>	area	km ²	1.6	2.1
<i>w</i>	width	m	3.3±0.8	3.2±0.47
<i>S</i>	slope	rise:run	0.82°	0.96°

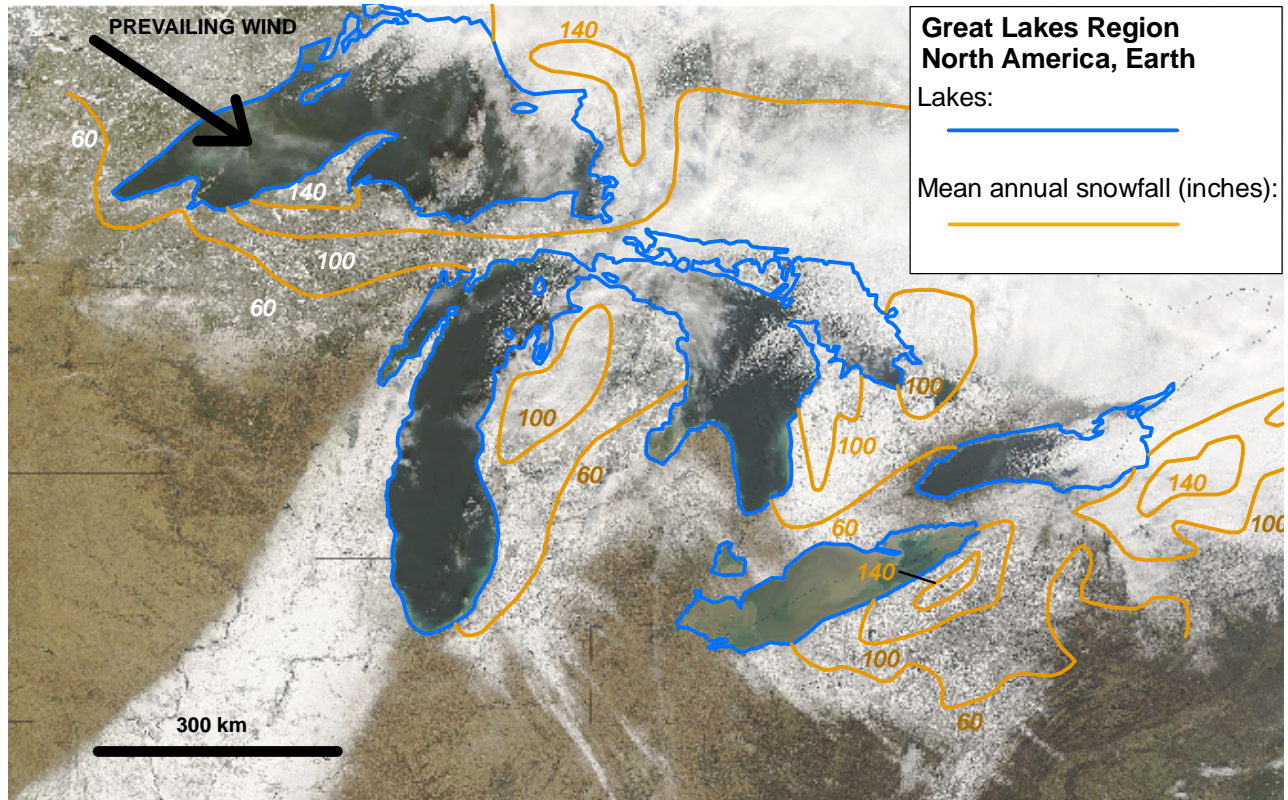
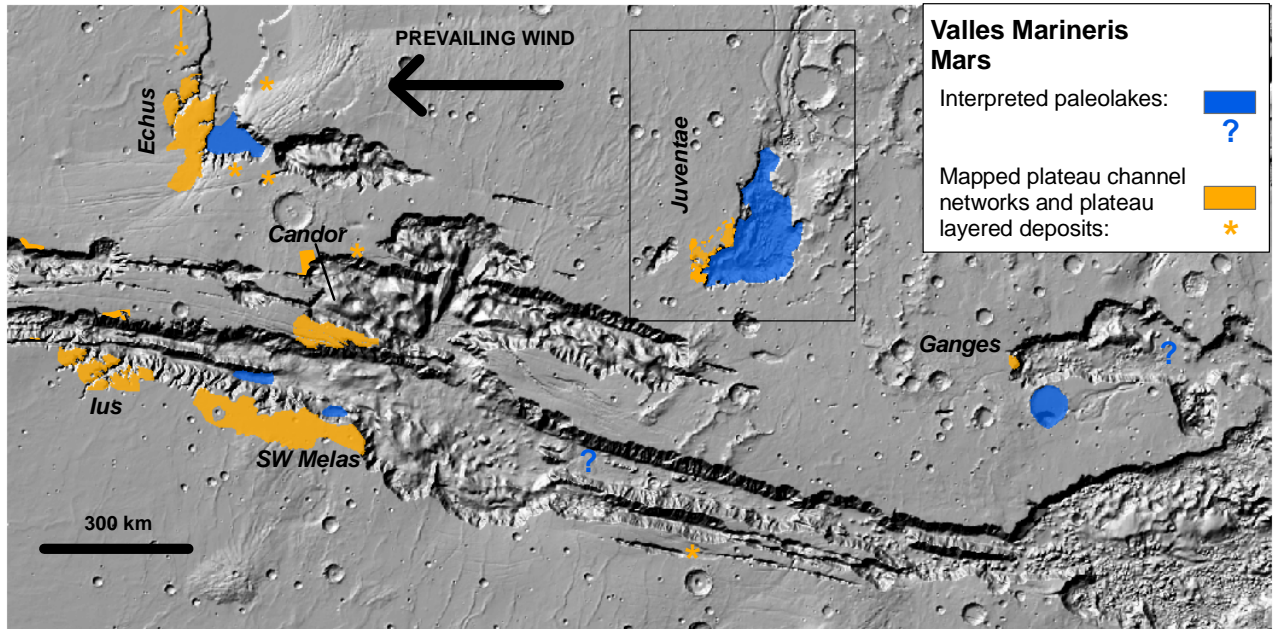


Figure 1. (Upper panel) Location of Valles Marineris plateau layered deposits and plateau channel networks downwind of paleolakes. Reported plateau layered deposits and channel networks are shown by orange shading. Asterisks correspond to isolated, or incompletely mapped, occurrences. Reported paleolakes are shaded in blue: those where we consider the evidence to be less strong are shown by question marks. Box around Juventae corresponds to Figure 4. Background is MOLA shaded relief. Sources:- *Weitz et al.* [2010] (SW Melas, S Ius, S flank W Candor, Juventae and Ganges layered deposits); *Le Deit et al.* [2010] (N Ius, N flank W Candor, N Tithonium and Juventae layered deposits) *Mangold et al.* [2008] (Echus networks); *Williams et al.* [2005] (Candor channel); *Harrison & Chapman* [2008] (questionable Candor lake); *Harrison & Grimm* [2008] (Juventae and Echus lakes); *Metz et al.* [2009] (SW Melas lake); *Roach et al.* [2010] (Ius closed evaporitic basin); *Komatsu et al.* [2009] (Morella lake). The questionable Ganges lake is our own interpretation. (Lower panel) Location of snowbelts downwind of the Great Lakes, North America, Earth. Each local maximum in mean annual snowfall, as shown by orange contours, is downwind of a lake. Snowbelts form from the cumulative effect of lake-effect storms. Contours are from [*Eichenlaub*, 1979], as reproduced in *Markowski & Richardson* [2010]. The prevailing wind direction is shown by the black arrow and the snow streaks in the background image. Background image was acquired 9 December 2006 by Terra/MODIS and shows the effects of a lake-effect storm on 7-8 December 2006 (image credit: NASA GSFC/Earth Observatory).

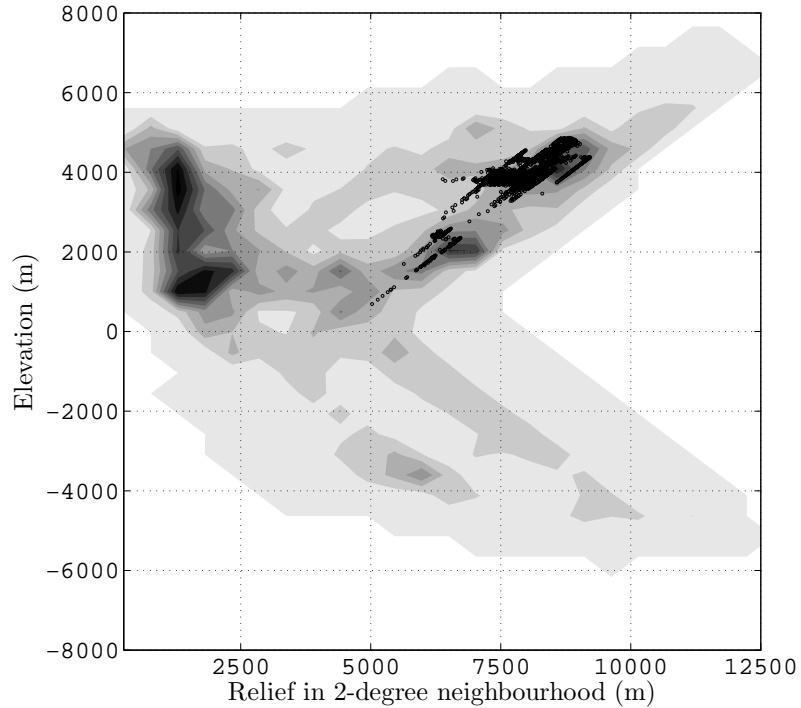


Figure 2. Topographic context of inverted channels. Black dots correspond to points mapped as ‘light-toned layered deposit’ or ‘inverted channel’ by *Weitz et al.* [2010]. The association of inverted channels with light-toned layered deposits containing opal \pm jarosite is only found near the rims of large canyons. Grayscale background is the probability distribution of all points, using a bin size of 500m. Relief at a point is defined as the maximum difference in elevation between that point and all other points in a neighbourhood with 2-degree radius. (Points with intermediate elevation cannot have high relief with this definition.)

0. INFERENCE FROM GEOLOGIC RELATIONS:

FORMATION OF PLATEAU CHANNELS AND PLATEAU LAYERED DEPOSITS IS LINKED TO CHASM OPENING (AND ASSOCIATED FLOODING).

1. SCENARIOS THAT COULD ACCOUNT FOR THIS LINK:

A) EARLY FORMATION

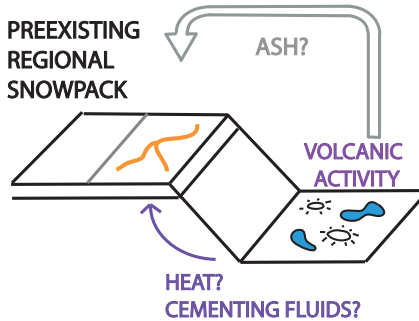
CHANNELS FORM EARLY IN CHASM OPENING



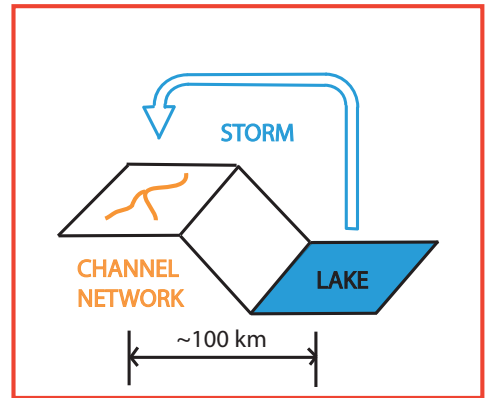
MOST ARE DESTROYED BY FURTHER CHASM GROWTH

B) WIDESPREAD SNOW OR ICE, LOCALIZED MELTING AND/OR PRESERVATION.

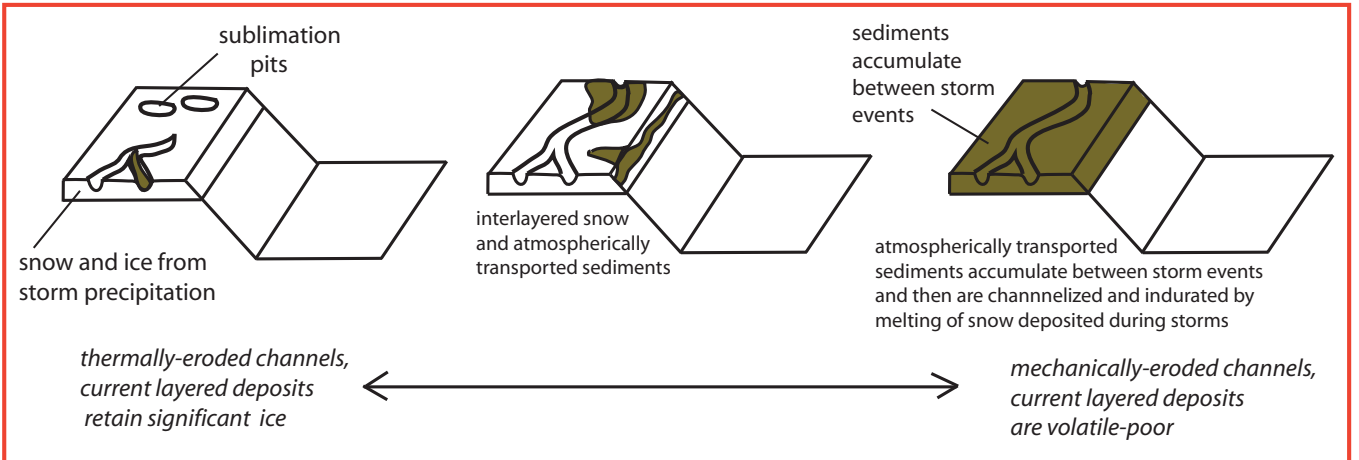
PREEXISTING REGIONAL SNOWPACK



C) WATER-LIMITED FORMATION (PREFERRED SCENARIO)



2. POSSIBLE CHANNEL-FORMING MECHANISMS WITHIN PREFERRED SCENARIO



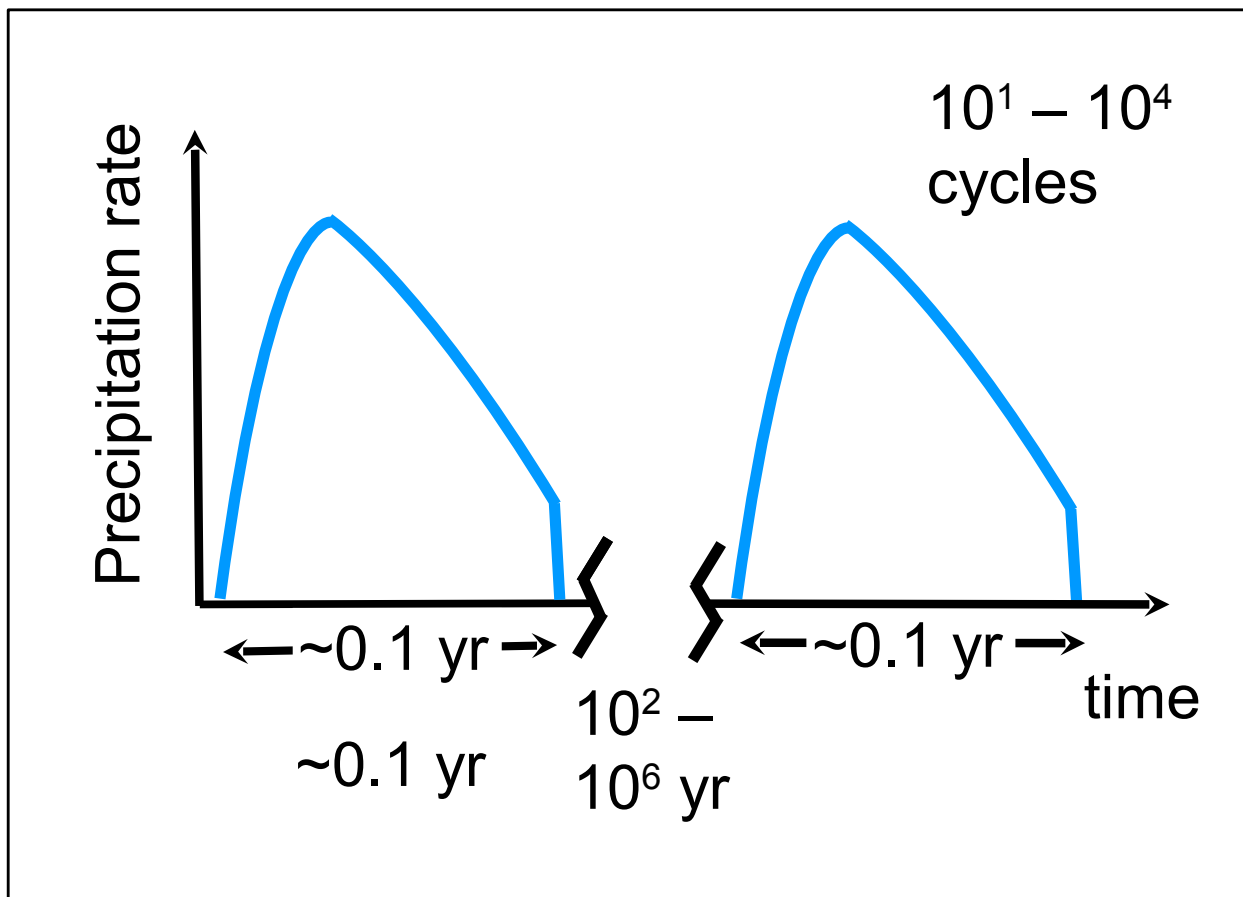


Figure 3. Top panel: Sketch of our hypothesis. Condensation of vapor released from short-lived lake in chasm creates a snowstorm. Precipitation on the plateau next to the chasm forms channel networks. Precipitation falling back into the lake leaves no geomorphic signature. Boxed inset shows the timescales implied by published models of chaos hydrology and the thermodynamics of lake freezing: each lake event lasts ≤ 1 year [Andrews-Hanna & Phillips, 2007; Harrison & Grimm, 2008]. Crosscutting channels, and discharge estimates from measurements of inner channels, require that many flood events occurred in each chaos chasm. Bottom panel: Estimates of repose interval between groundwater outflow events center on $10^2 - 10^6$ years, and are considered to lengthen with time, but are sensitive to poorly-known crustal hydrologic properties [Andrews-Hanna & Phillips, 2007; Harrison & Grimm, 2008].

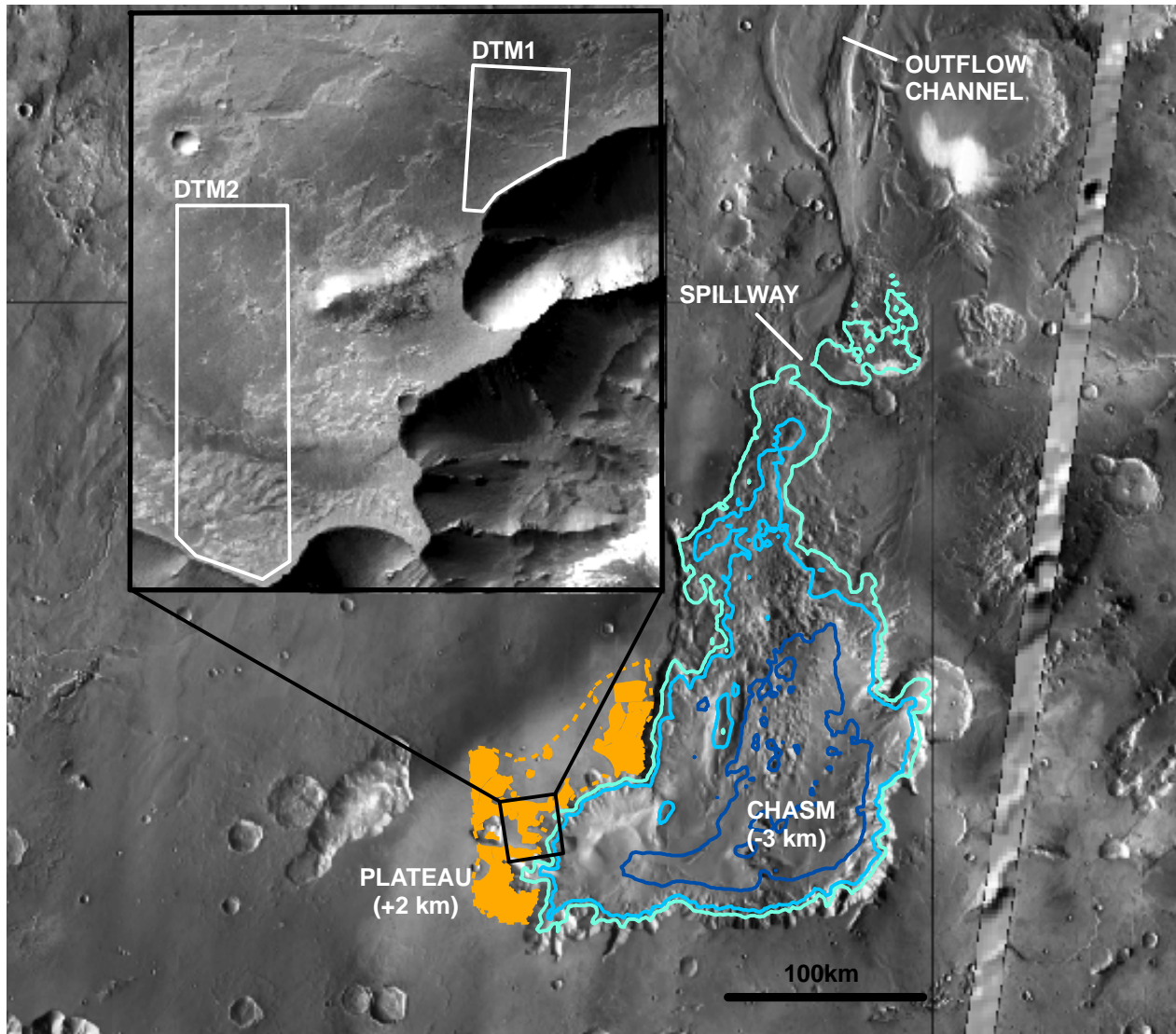


Figure 4. Site for our hypothesis test – Juventae. Juventae Chasma is a 5 km deep, sharp-sided chaos chasm that sources Maja Valles (outflow channel to N). *Main image:* Orange shading corresponds to the area of plateau channel networks and plateau layered deposits mapped by *Le Deit et al.* [2010]. Orange dotted line corresponds to pre-erosion extent estimated by *Le Deit et al.* [2010] from outliers. Spillway to N of chasm indicates that flood level exceeded +1180m. We model flooding to depth -3000m (deep blue), -1000m (mid blue) and +0m (cyan). Main figure background is THEMIS VIS mosaic. *Inset image* shows the locations of 2 HiRISE DTMs (supplementary online data) that we constructed to characterize the hydraulic geometry and stratigraphic context of the inverted channel networks. Inset background is part of CTX image P18_007983_1751_XN_04S063W.

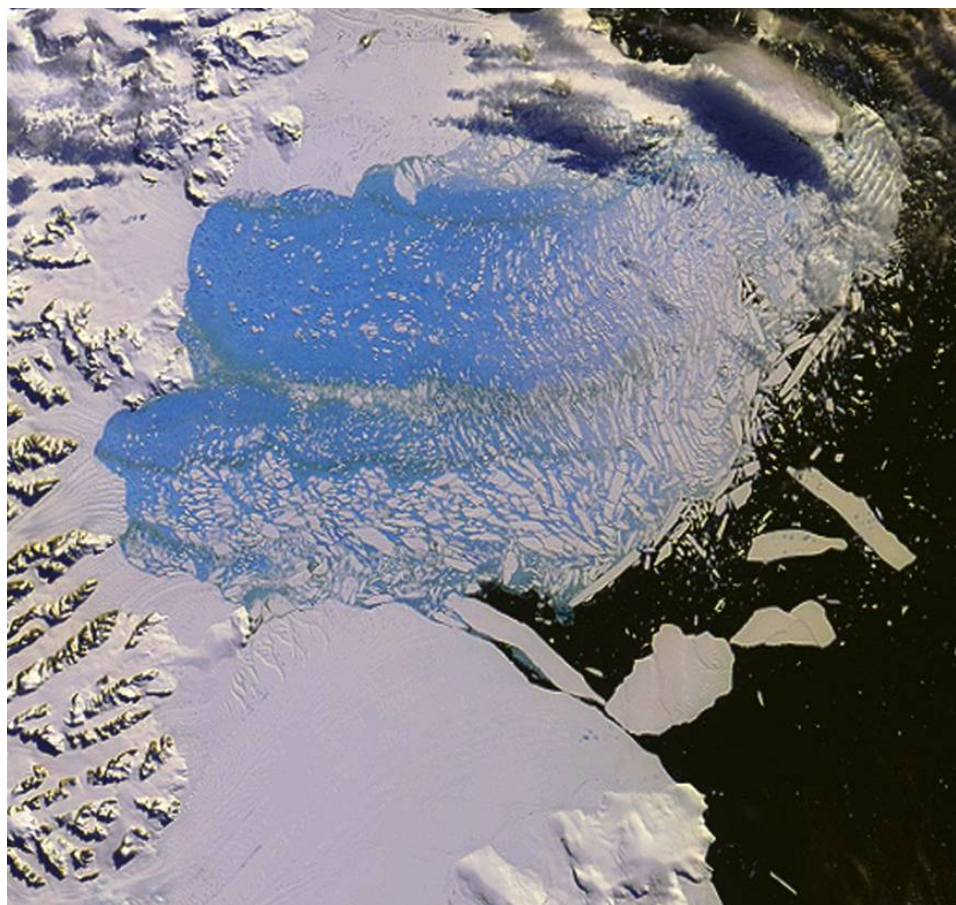


Figure 5. Disintegration of Antarctica's Larsen B ice shelf. Collapsed area is ~ 3000 km². Acquired 7 March 2002 by Terra/MODIS. Image credit: NASA/GSFC.

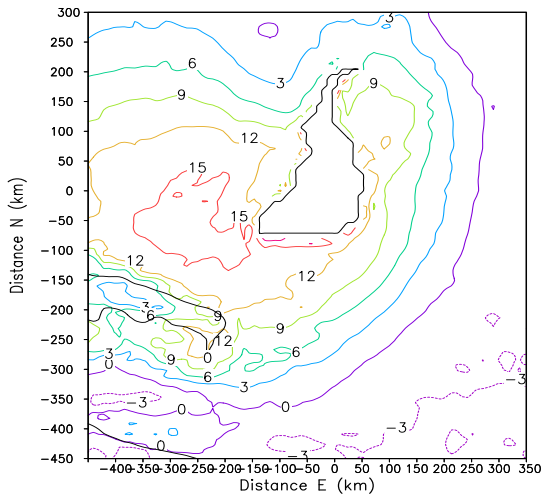
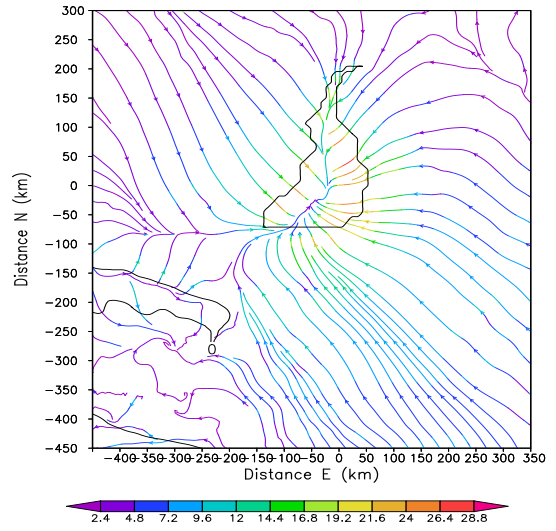
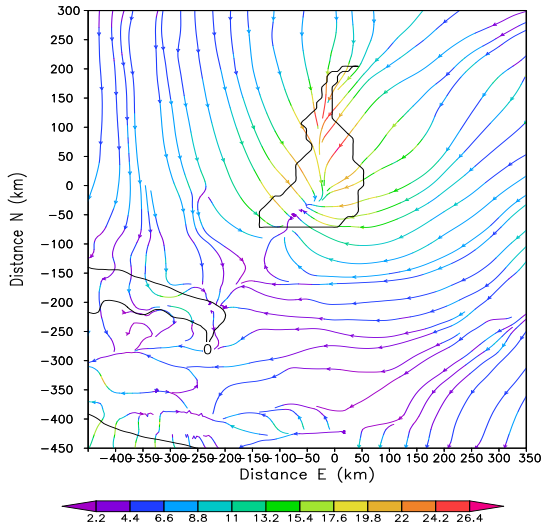


Figure 6. Temperature and wind field at Juventae in our best-fit lake simulation (`juventae_high`). 0m contour (black) defines canyons. (a) Net time-averaged wind at 13m elevation. Overall Easterly & South-Easterly winds are reversed at Juventae Chasma because of the lake-driven circulation (b) shows change in wind field due to the lake (differencing dry and wet runs). Lake storm drives low-level convergence of up to 30 m s^{-1} . Magnitude of lake-driven circulation is comparable to magnitude of non-lake circulation. (c) Temperature difference due to lake. Temperature increases by up to 18K downwind of the lake. Axis tick labels correspond to distance from 3.91S 298.53E, near the lake center (Note: `juventae_high`, average over 3 sols, from Mars-hours 49 to 121).

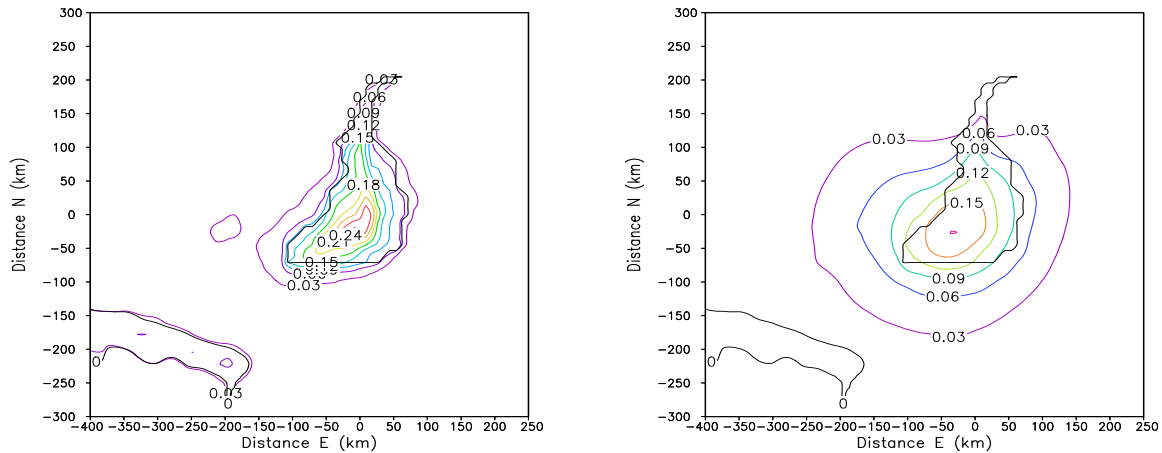


Figure 7. Ice and vapor columns at Juventae Chasma. (a) Time-averaged precipitable vapor column abundance in cm water equivalent. (b) Time-averaged precipitable ice column abundance in cm water equivalent. (Note: `juventae_high`, Average for 3 sols, from Mars-hours 49 to 121).

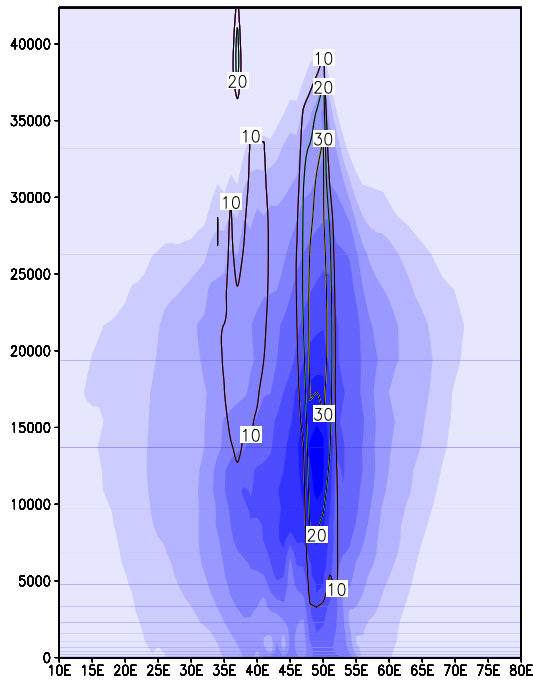


Figure 8. E-W cross section through lake storm. Blue tint corresponds to increasing water ice fraction (interval 0.001, maximum value 0.009). Labeled contours correspond to bulk vertical velocity in m s^{-1} , which are comparable to the most intense supercell storms on Earth. The y-axis is vertical distance in m. The x-axis is horizontal distance: 10 units = 83 km. Lake extends from 41E to 55E on this scale.

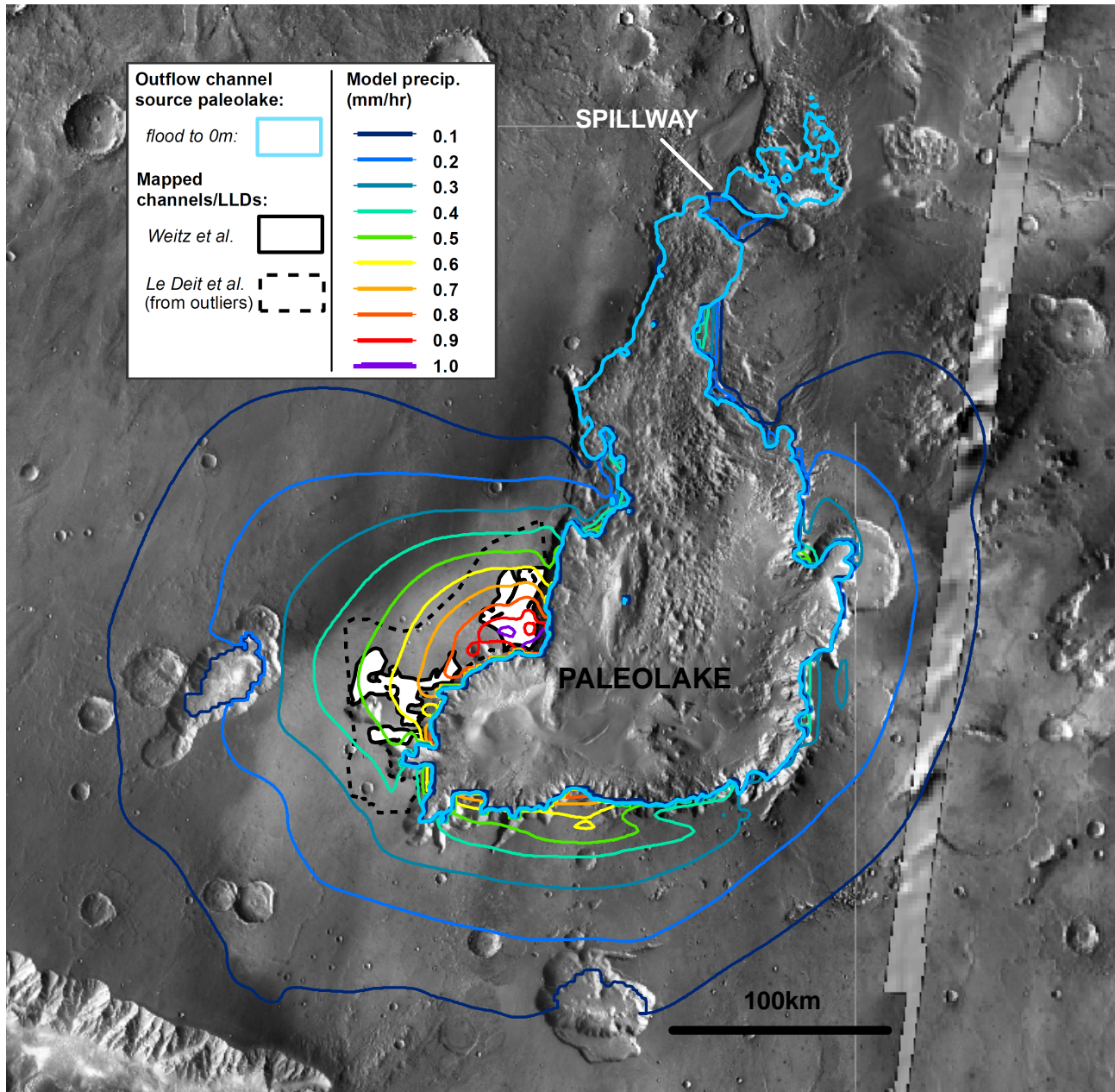


Figure 9. Modeled precipitation contours overlain on observed geology at Juventae. White shading with thick solid black outline corresponds to area of layered deposits and inverted channels reported by *Weitz et al.* [2010]. The dashed black line corresponds to the pre-erosion area of layered deposits inferred from outlier buttes and pedestal craters by *Le Deit et al.* [2010]. The thick cyan line defines the flooded area for this simulation (the -1000m contour). The colored lines are modeled time-averaged precipitation contours at intervals of 0.1 mm/hr water equivalent. Precipitation falling back into the lake is not shown. The spatial maximum in mean precipitation is ≈ 1.0 mm/hr. (Note: sol 5 average).

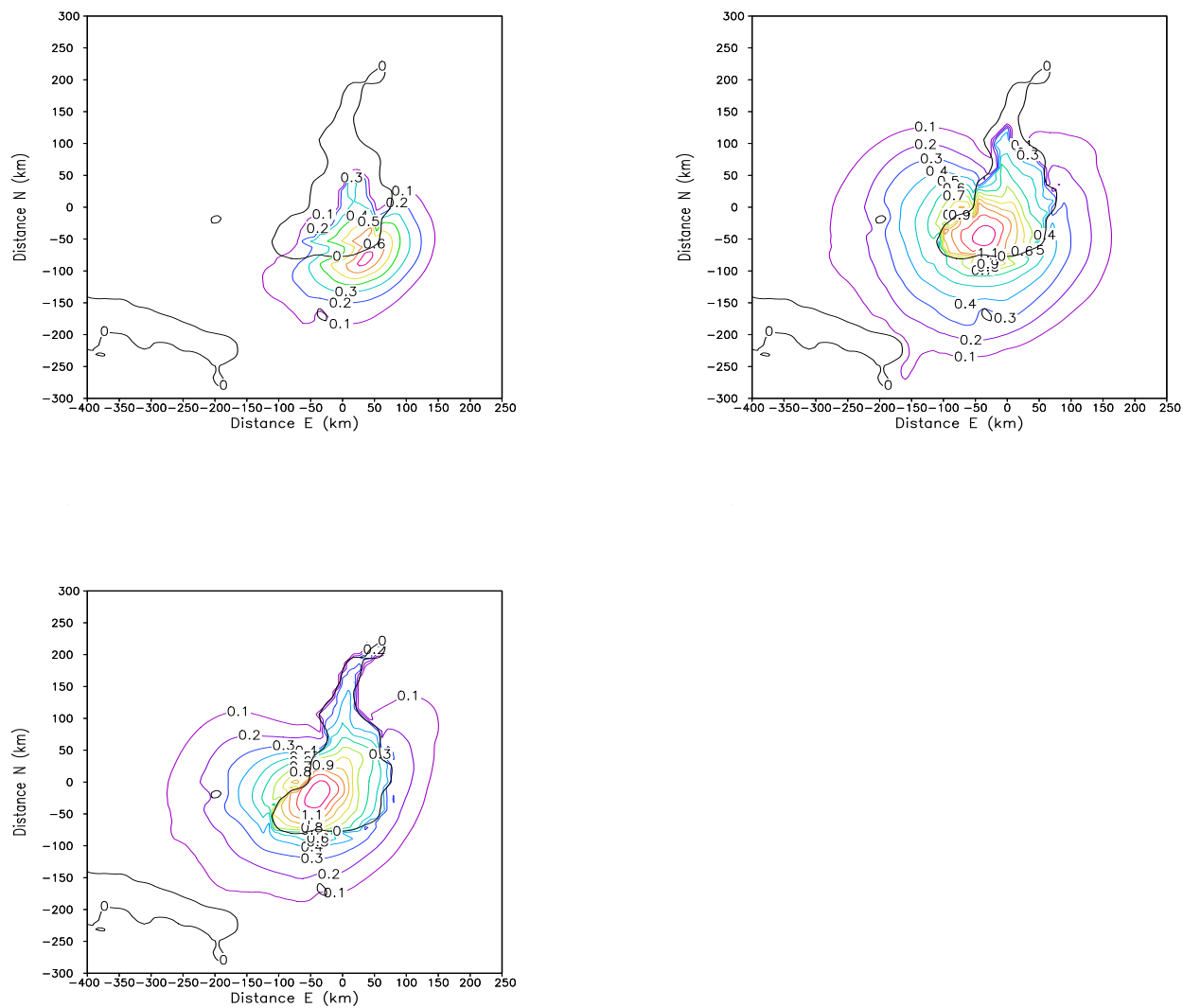


Figure 10. Sensitivity test comparing mean precipitation (mm/hr) for 3 different lake levels. a) -3000m (*juventae_low*), b) -1000m (*juventae_medium*), c) 0m (*juventae_high*).

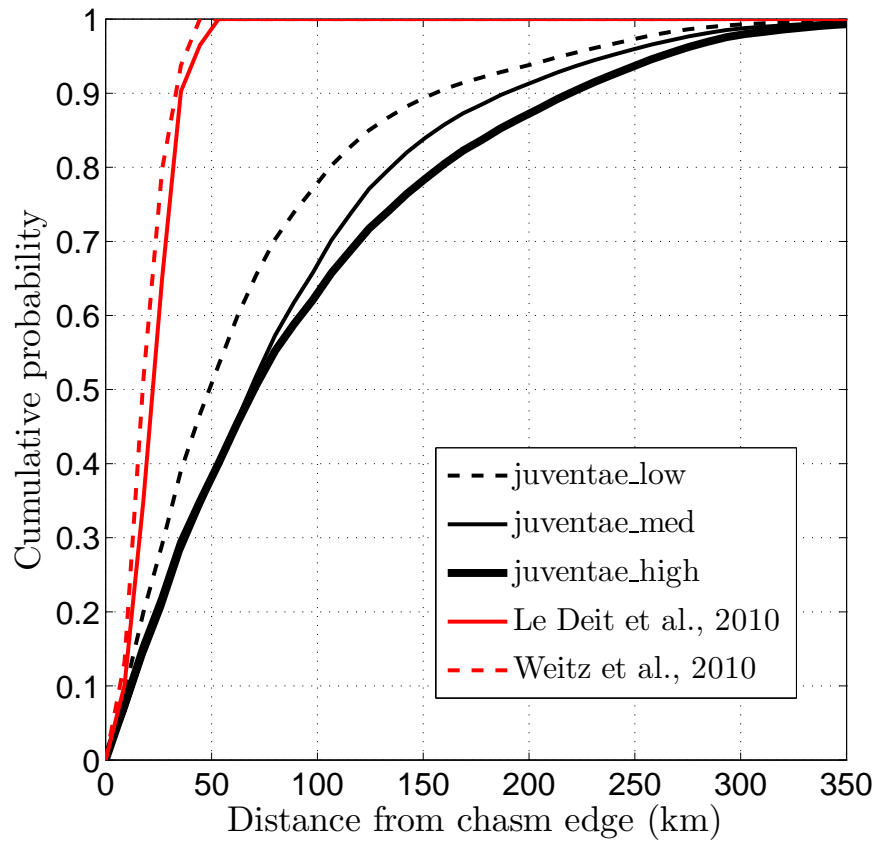


Figure 11. Comparison of falloff of precipitation with falloff of mapped area of channels and layered deposits. Because of an arbitrary mapping cutoff, layered deposits likely extend further than shown.

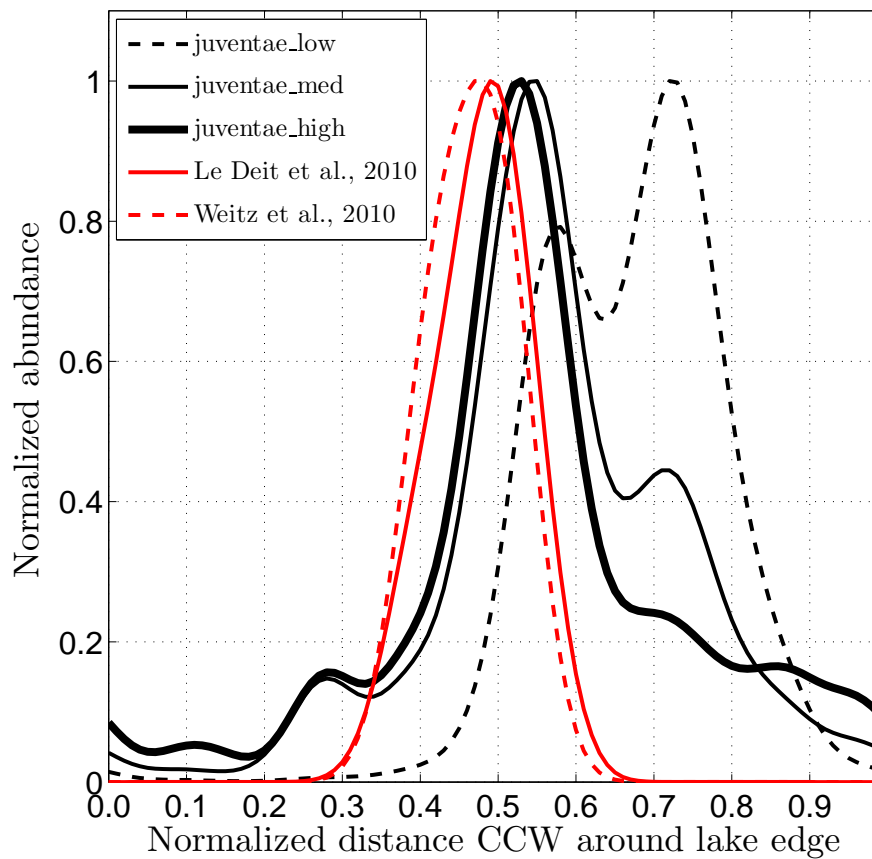


Figure 12. Comparison of azimuth of precipitation with azimuth of mapped channels.

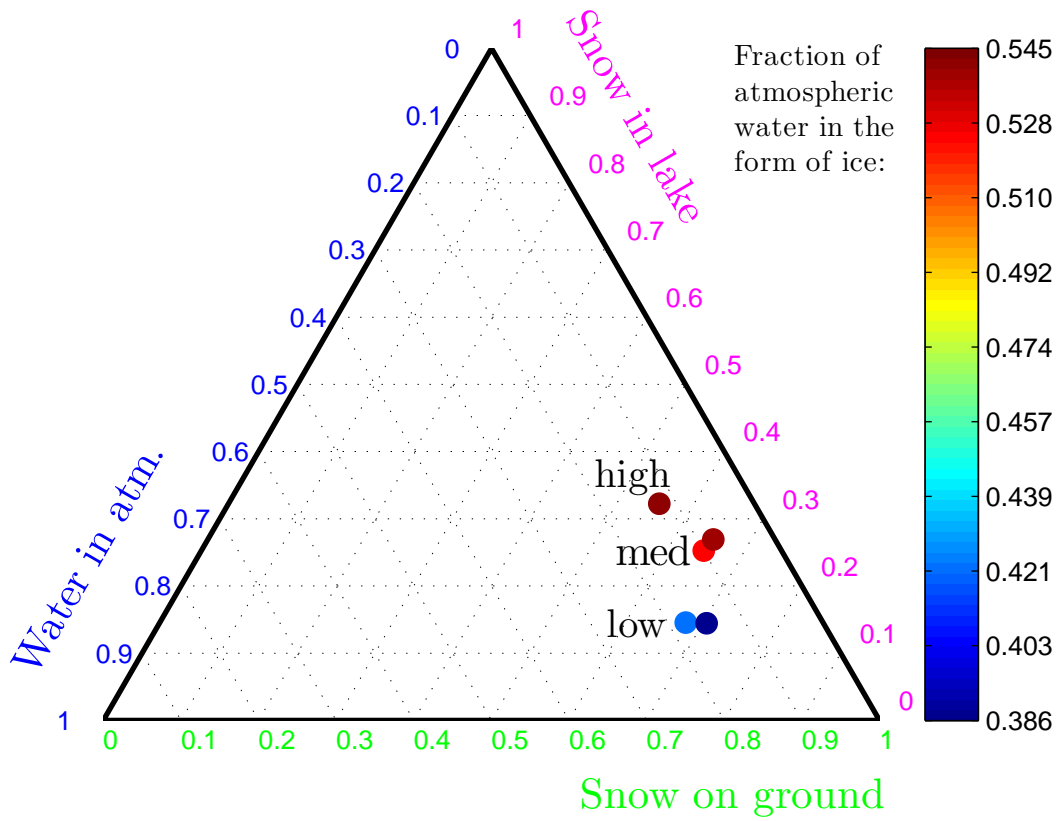


Figure 13. Fate of vapor released from the lake (precipitation efficiency). Colored dots corresponds to simulations' inventory of water (ice + vapor) after either 5 or 7 sols, after subtracting the inventory of a lake-free run. Color corresponds to fraction of atmospheric water in the ice phase: red is more ice-rich, blue is more vapor-rich. Only snow on ground can contribute to localized geomorphology. Water vapor in the atmosphere can contribute to regional and global climate change: greenhouse warming is increasingly likely as the mass of atmospheric water increases.

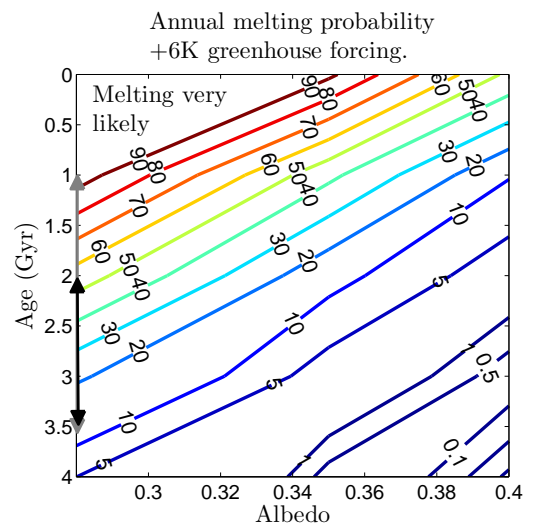
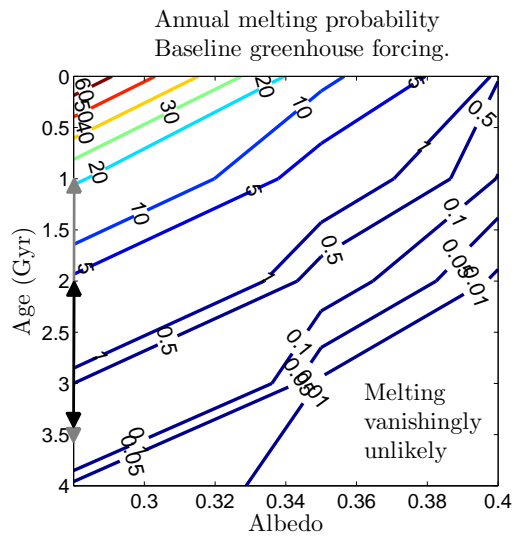


Figure 14. Equatorial melting probability (%) for flatlying snowpack and solar luminosities appropriate to 0 to 4 Gya. Gray arrow on the y-axis corresponds to the range of ages for opaline layered deposits stated in the text of *Murchie et al.* [2009a]. Black arrow corresponds to the smallest range of stratigraphic ages that could accommodate all the plateau channel networks according to *Le Deit et al.* [2010]. These ranges are large because of the uncertainties in mapping crater counts onto absolute ages [*Hartmann, 2005*], and it is possible that all the plateau channel networks formed at roughly the same time.

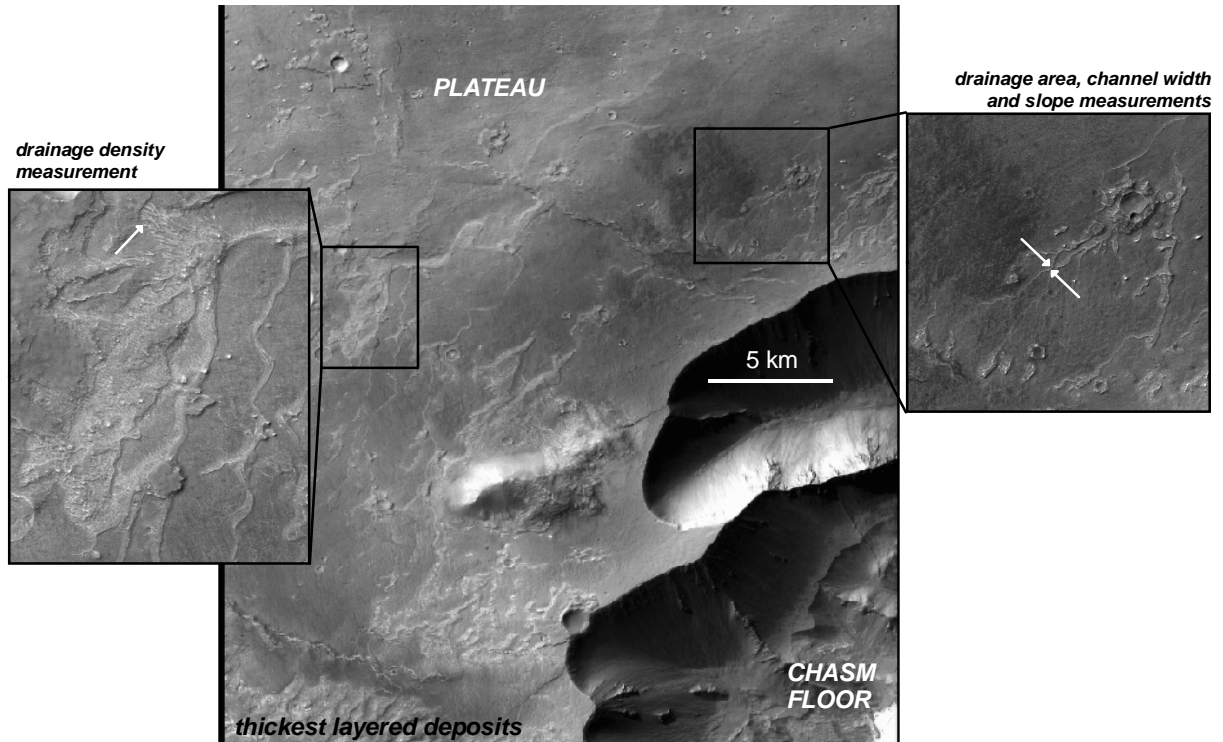


Figure 15. Geological context of measurements of layered deposit thickness, channel drainage density, catchment area, channel slope and channel width. White arrows in zoomed-in panels show localities. Some thickness measurements come from an area just SW of this image. Background is part of CTX image P18_007983_1751_XN_04S063W.

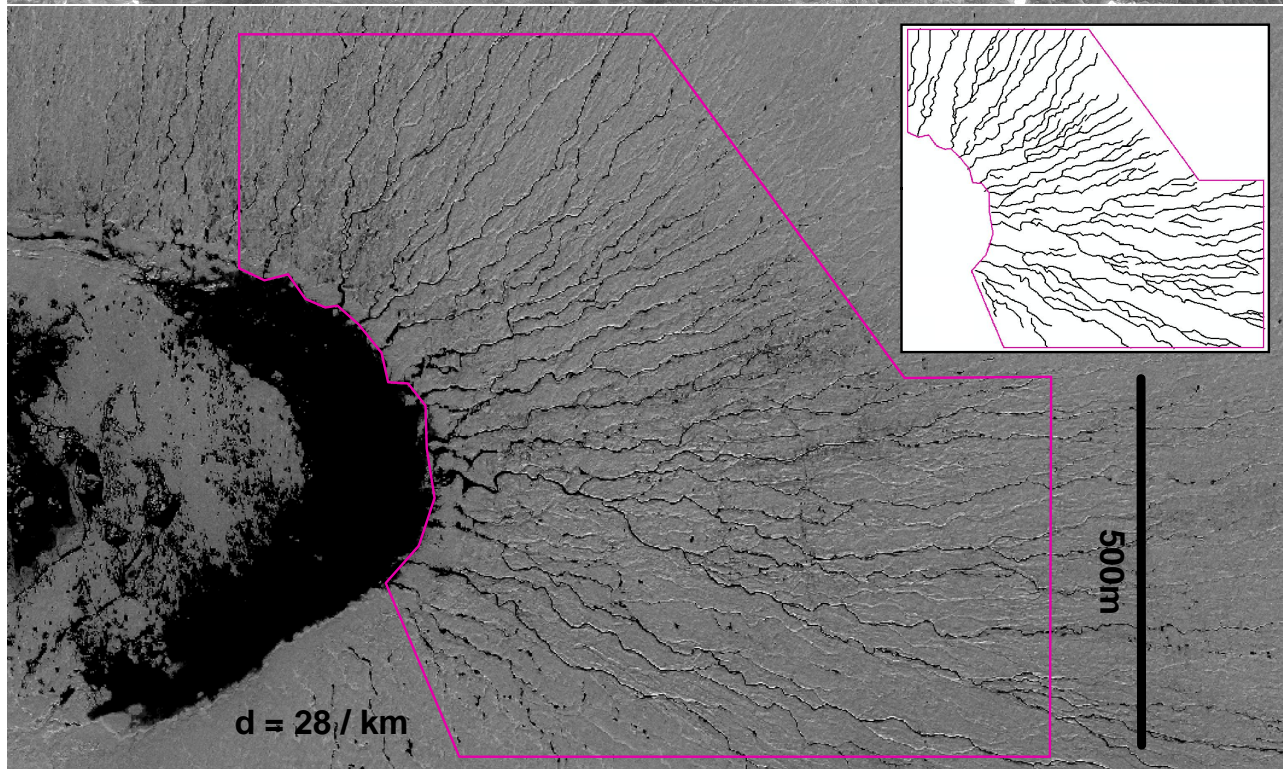
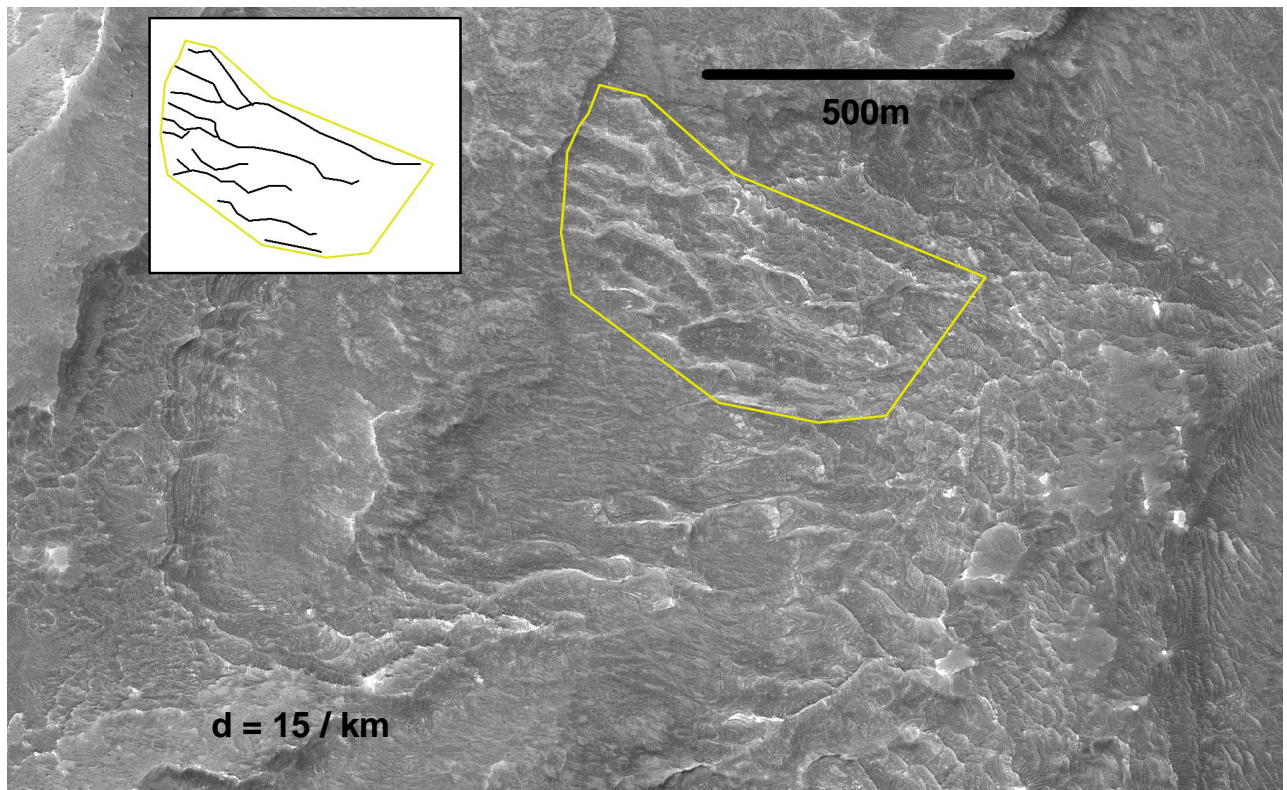


Figure 16. Maximum drainage density, d , at Juventae ($d = 15 \text{ km}^{-1}$) is less than drainage density for snowmelt-carved systems on the Greenland ice plateau ($d = 29 \text{ km}^{-1}$). Polygons enclose the area for which the drainage density was measured, and the inset panels show channels which contributed to the count. *Upper panel:* PSP_005346_1755, Juventae Plateau. This locality was identified by *Malin et al.* [2010] as “the best evidence yet found on Mars to indicate that rainfall and surface runoff occurred.” *Lower panel:* IKONOS image of Greenland ice sheet, showing snowmelt-carved channels draining into a supraglacial lake. (Image courtesy Jason Box/OSU/Discovery Channel; *Box & Ski* [2007]). *Details:* Greenland - length = 21.3 km, area = 0.77 km^2 , giving $d = 28/\text{km}$. Mars - length = 3.4 km, area = 0.22 km^2 , giving $d = 15/\text{km}$.

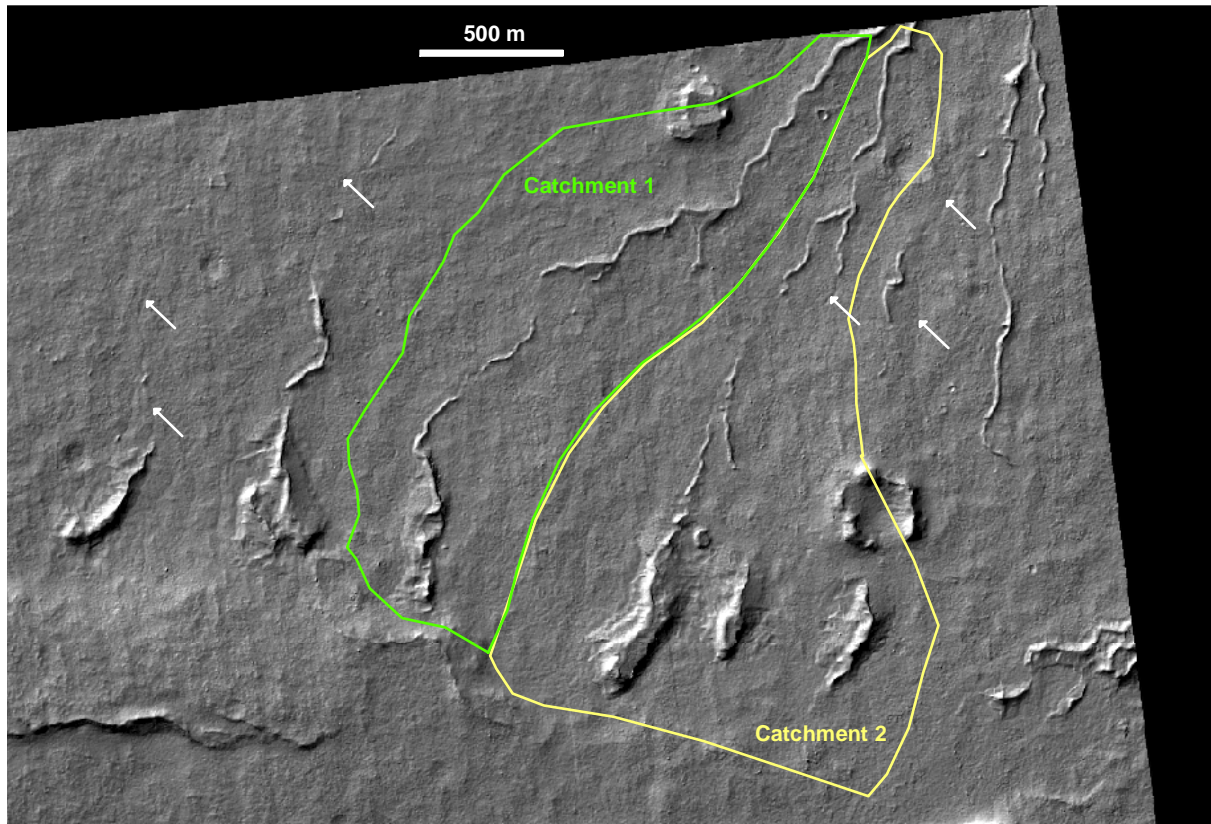


Figure 17. Inverted channel systems on the Juventae plateau from which hydraulic parameters were measured. Shaded relief from HiRISE stereo DTM 1 (Figure 4), illuminated from top left. North is up. Barely-visible striping parallel to the edge of the shaded relief raster is an artifact of stereo DTM generation. Inverted channel heights are typically 2-5m. Shallow negative-relief channels (white arrows, depth < 1 m from DTM) join some inverted channel segments. The corresponding HiRISE image pair is PSP_003223_1755 and PSP_003724_1755.

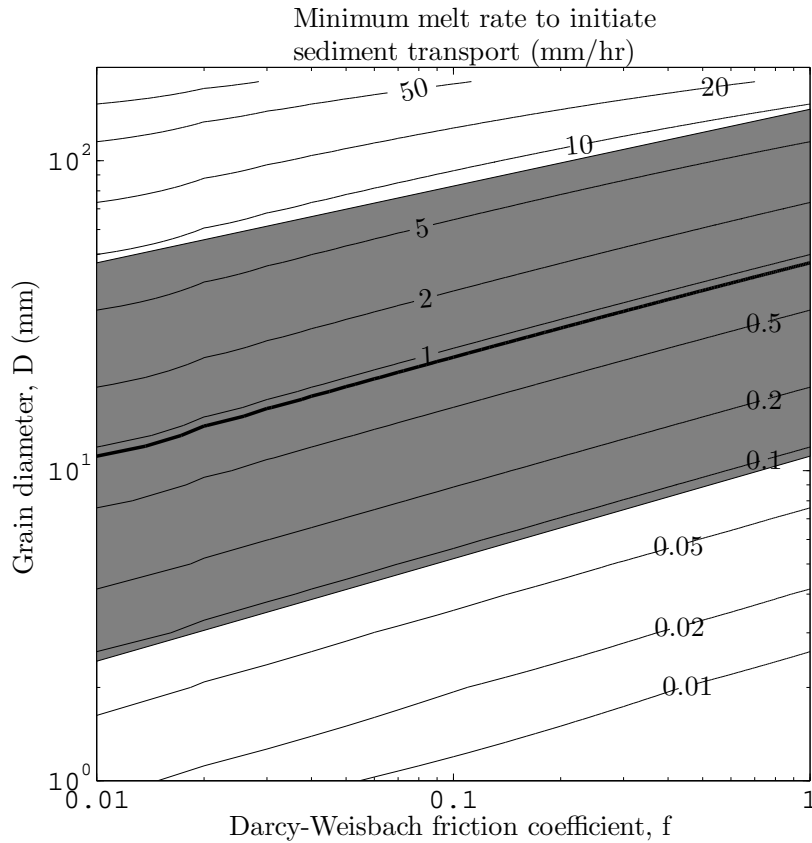
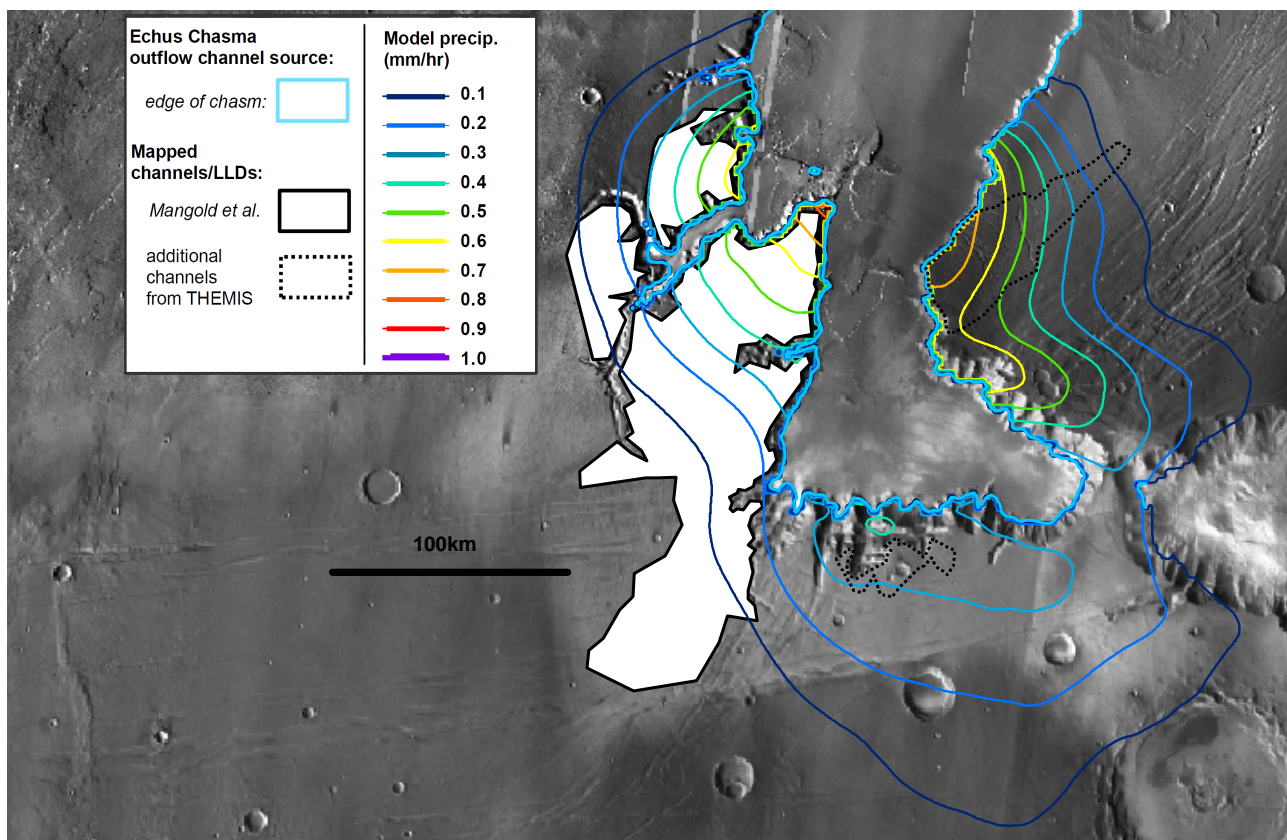


Figure 18. Grain sizes that can be mobilized by the modeled precipitation. The central black line corresponds to the modeled snowfall rate, 0.9 mm/hr. Because we consider the modeled precipitation rate to be only an order-of-magnitude guide to the true precipitation rate, the gray envelope shows order-of-magnitude errors in both directions. The melting rate will be lower than the precipitation rate, and in our probabilistic discharge model the exceedance probability for a melt rate of 1.0 mm/hr is extremely low. Melt rates of 0.09 mm/hr (lower end of gray envelope) are more likely, and are sufficient to mobilize sand and gravel.



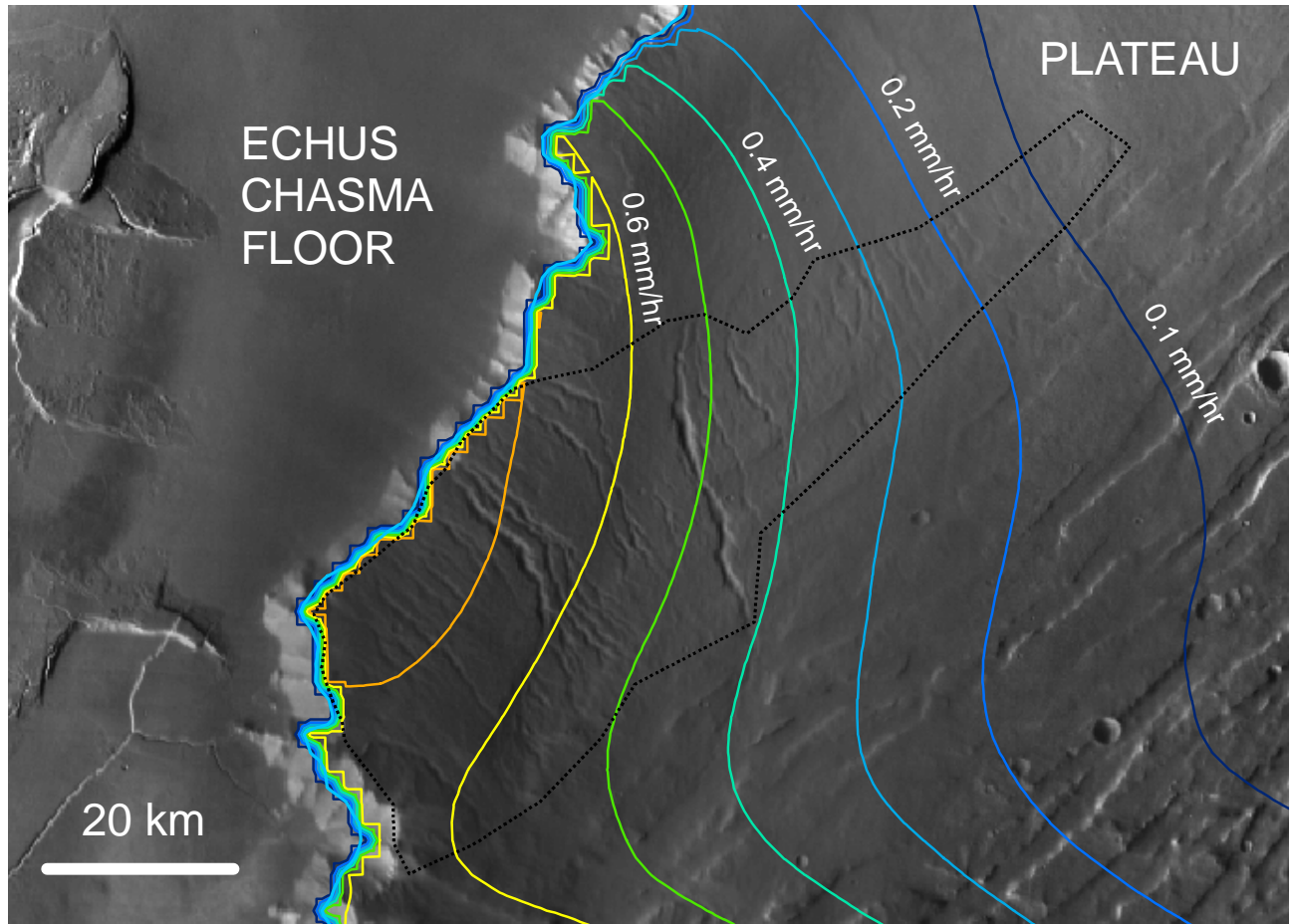


Figure 19. a) Modeled precipitation contours overlain on observed geology at Echus. White shading with thick solid black outline is the perimeter of channels reported by *Mangold et al.* [2008]. The dotted black line corresponds to additional channels observed in the THEMIS Day IR 100m per pixel global mosaic. The colored lines are modeled mean precipitation contours at intervals of 0.1 mm/hr water equivalent. Precipitation falling into the lake is not shown. b) Focus on area where channels have not been previously mapped. The dotted line encloses the area of channels visible in Themis IR mosaic. The depth and width of the observed channels decreases away from the chasm edge in step with the decline in modeled precipitation.